
Optical fiber cavities

Master thesis
from
Natalie Thau

angefertigt am
Physikalisches Institut der Universität Bonn

vorgelegt der
Mathematisch-Naturwissenschaftlichen Fakultät
der
Rheinischen Friedrich-Wilhelms-Universität Bonn

Oktober 2012

Gutachter

1. Gutachter : Prof. Meschede

2. Gutachter : Prof. Reichel

Contents

1	Introduction	3
2	Theoretical background	5
2.1	Optical fiber	5
2.2	Fiber mirror	7
2.2.1	CO ₂ laser	7
2.2.2	Ablation process	8
2.3	Fiber Fabry-Pérot cavity	9
2.3.1	Gaussian beams and the TEM ₀₀ mode	10
2.3.2	Properties of the optical cavity	11
2.3.3	Cavity spectrum	12
3	Fabrication of fiber mirrors in Paris	15
3.1	Fiber preparation	15
3.2	CO ₂ laser	15
3.3	Ablation setup	16
3.4	Ablation parameter	19
3.5	Characterisation of the profile on the fiber end facet	22
3.5.1	Mirau profilometer	22
3.5.2	Fizeau Profilometer	23
3.5.3	Mirror parameters	24
3.6	Minimization of the astigmatism	26
3.7	Reproducibility	28
3.8	Coating	30
4	Fabrication of fiber mirrors in Bonn	32
4.1	Ablation setup	32
4.2	Power stability and ablation parameters	33
4.3	Michelson profilometer	34
4.4	First characterisation	35
4.5	Fiber holder	36
5	Characterisation of a fiber cavity	38
5.1	Fiber Fabry-Pérot cavity	38
5.2	Characterisation setup	38
5.3	Alignment	39
5.4	Characterisation	40
5.4.1	Cavity length, free spectral range and finesse	41
5.4.2	Mirror reflectivity, mode waist and cavity decay rate	42
5.4.3	Resonance splitting	43
5.4.4	Discussion	44
6	Summary	45

7 Appendix	47
A Circuit diagramm of the control of the ablation process	47
Literaturverzeichnis	49

1 Introduction

Edward Mills Purcell has predicted in 1946, that the spontaneous emission probability of an atom increases significantly if the system is placed in a cavity with one of its modes resonant with the nuclear transition of the atom [1]. This is commonly regarded as the foundation of cavity quantum electrodynamics and enables the exploration of the fundamental aspects of light-matter interaction, and especially for our group, the realisation of a fast and stable control of this interaction as a basic tool for quantum communication. For our experiments cesium and rubidium are mainly used since their transitions are accessible by lasers. With the improvement of the trapping methods for atoms and molecules [2] [3], the vacuum systems and the cooling mechanisms [4],[5] in combination with a microcavity the coherent interaction between single photons and internal atomic states of cesium was first observed in 1992 [6] and then for rubidium atoms in 1996 [7]. With the further improvement of quantum state transport [8] and a submicrometer positioning of atoms inside the cavity [9], the atoms can be controllably placed in the mode waist.

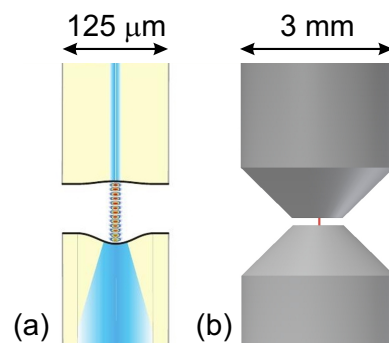


Figure 1.1: Fabry-Pérot cavity made of (a) fiber mirrors (group of Prof. Reichel, LKB, Paris) and (b) superpolished mirrors (group of Prof. Meschede, IAP, Bonn). Rubidium atoms (a) or cesium atoms (b) trapped in the cavity interact with the light field if one of the cavity modes is resonant with the nuclear transition of the atom.

The present experiments can couple cesium or rubidium atoms to a cavity as shown in Fig. 1.1 consisting of two highly reflective mirrors between which a light field is applied. The interaction between atoms and the mode field of the cavity is quantified by the coupling rate which defines how frequent a photon is coherently absorbed by the atom and reemitted into the light field. The system is strongly coupled if this coherent energy exchange is faster than the decay rates of the atomic dipole and the cavity field and therefore the process behaves periodically. Our approach to enter this regime is as follows: On one hand we reduce the cavity field decay rate. To do this, we produce mirrors with a very low surface roughness down to a few Ångströms and with highly reflective dielectric coatings which provide a large finesse up to 10^6 . On the other hand we increase the coupling rate by using a small mode volume which is achieved by the fabrication of mirrors with a small radius of curvature. In Bonn we use a cavity made of super polished mirrors with radii of 5 cm fabricated on a coned glass substrate [10] and in Paris a cavity made of fiber mirrors with radii of $250 \mu\text{m}$ fabricated with a CO_2 laser beam [11]. Only for the fiber mirrors is the lower limitation for the radius not yet reached. Thus, a cooperation between the group of Prof. Reichel (LKB, Paris) and the group of Prof. Meschede (IAP, Bonn) was established. In this work the fabrication of fiber mirrors was developed further at the original ablation setup in Paris with the goal of a higher efficiency and a higher controllability of the process. An improved ablation setup was then built up in Bonn to fabricate mirrors for

a new cavity experiment.

In a different experiment we built up a fiber cavity in Paris to investigate the cavity birefringence which is observed as a resonance splitting in the transmission signal and is caused by intrinsic stress in the mirror coating. This splitting in the MHz-regime can cause the coupling of the mode field to two different atomic states or disturb the Doppler cooling which depends on the atom-field detuning. Furthermore the resonances corresponds to two linearly polarised orthogonal modes. Since the coupling rate is proportional to the dipole moment of the atomic transition, the outer Zeeman transitions with the largest dipole moment [12] that only couple to circularly polarised light, are preferred as shown in Fig. 1.2 for cesium. Therefore, the resonances have to be overlapped to couple in σ^+ or σ^- light.

In this thesis the improvement of the ablation setup in Paris are presented first, following by the discussion of the new setup in Bonn and finally the methods and results of the characterisation of a fiber cavity in Paris.

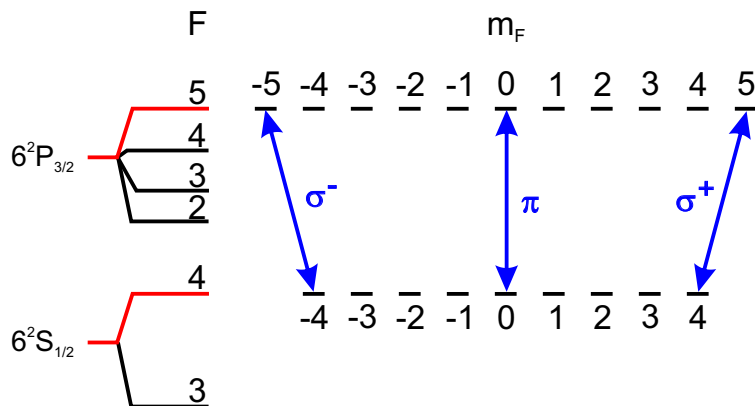


Figure 1.2: Level scheme of cesium with the relevant Zeeman transitions. The transition between $F=4$ and $F=5$ is near-resonant with the cavity mode. The largest dipole moment for circularly polarised light (σ^+, σ^-) is 1.3 times larger than the largest dipole moment for linearly polarised light (π) [12].

2 Theoretical background

The topic of this chapter is the theoretical introduction of the fabrication of a fiber mirror starting with different types of optical fibers. Moreover, the stability criteria and the optical properties of a fiber Fabry-Pérot cavity are discussed.

2.1 Optical fiber

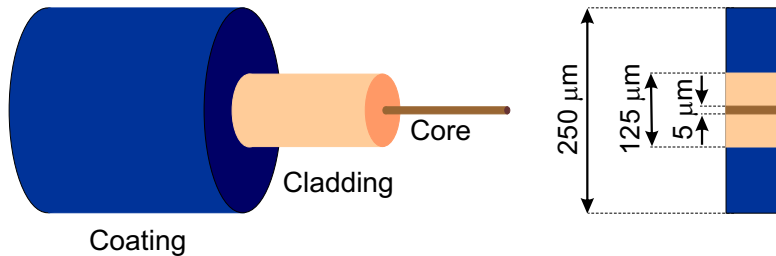


Figure 2.1: Schematic of a singlemode fiber: The fiber consists of a core, a cladding and a coating. Common values are shown in the cross section of the fiber.

Optical fibers are flexible waveguides, which transmit light with low losses down to 0.2 dB/km at a wavelength around 1550 nm as shown in Fig. 2.2. Therefore, they suits very well for atom experiments with transitions around 700 – 900 nm as shown in Fig. 2.3. A fiber consists of a fiber core and a cladding made of fused silica as shown in Fig. 2.1. The core is usually doped with germanium or boron to increase the refractive index n_{core} with respect to the cladding n_{clad} . The light is hence guided in the core with a radius r_{core} by total internal reflection. Below a certain frequency the mode decays exponentially instead of propagating in the core along the fiber axis since they radiates out of the fiber core. The so-called cut off frequency ω_c is defined by the numerical aperture NA and the p^{th} root x_{mp} of the Besselfunction $J_m(x)$ with $x = k_0 r_{\text{core}} \text{NA}$:

$$\omega_c = c \frac{x_{mp}}{r_{\text{core}} \text{NA}} \quad \text{with} \quad \text{NA} = \sqrt{n_{\text{core}}^2 - n_{\text{clad}}^2}. \quad (2.1)$$

Here m and p denote the angular and radial dependencies of the guided mode respectively. The operating wavelength is typically 100 nm beyond the cut off wavelength. A further relevant physical quantity is the mode field diameter (MFD), which is defined as the $1/e^2$ optical field diameter of the gaussian shaped fundamental mode. The MFD is always larger than the core diameter and depends on the wavelength. Finally the fiber is protected by one or two layers of coating. This is usually an acrylate or a copper jacket.

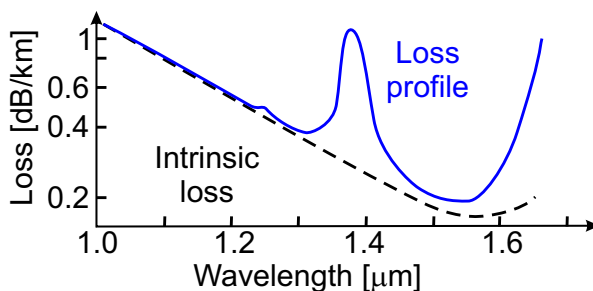


Figure 2.2: Loss spectrum of a singlemode silica fiber. The dashed line shows the contribution resulting from Raleigh scattering. Sketch from [13].

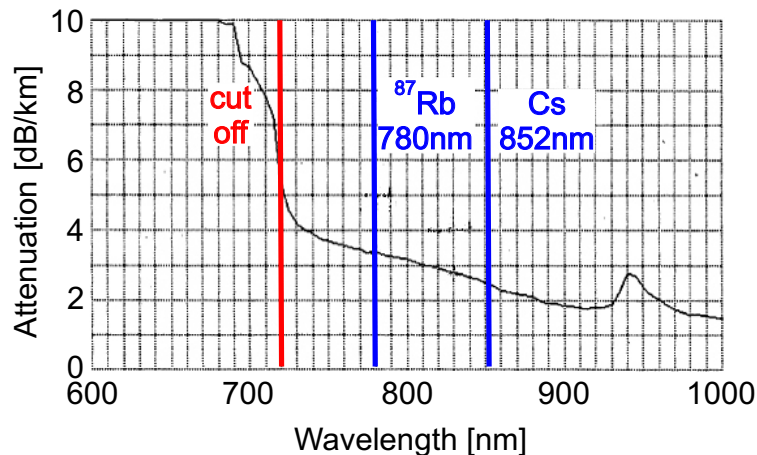


Figure 2.3: Performance of a single-mode fiber (SM800-5.6-125): The attenuation increases drastically below the cut off wavelength of 720 nm. This singlemode fiber is suitable for cavity experiments with ^{87}Rb and Cs atoms [14].

Fiber geometries

The cavity described in chapter 5.1 consists of a singlemode and multimode fiber. Both fiber types have a cylindrical shaped core and a homogenous cladding as shown in Fig. 2.4 (a) and (b). A fiber is called singlemode if the cut off frequency is $\omega_c(x_{01} = 2.405)$ and only the lowest-order mode is supported which doesn't have a cut off frequency (Fig. 2.3). All fibers with $\omega_c(x_{nm} > 2.405)$ are called multimode since these fibers support also higher modes than the fundamental mode. Associated with this is a much larger core radius compared to the singlemode fibers. Perturbations like temperature gradient or stress in the fiber can change the polarisation since two orthogonal polarisation states are degenerated. In the characterisation setup described in chapter 5.2 a polarization maintaining (PM) singlemode fiber is used. In this case of a PM fiber the refractive index of the two transverse axis is different due to an asymmetric geometrical structure of the core or an asymmetric induced permanent mechanical load in the cladding as sketched in Fig. 2.4.(c). This defines the slow axis with a smaller refractive index compared to the fast axis and the polarisation axis of linear polarised light, that is coupled into the fiber, has to be adjusted to the slow axis.

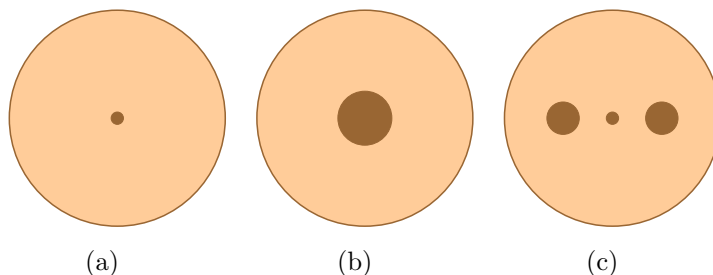


Figure 2.4: Cross section of different types of fibers: (a) singlemode fiber, (b) multimode fiber, (c) polarisation maintaining singlemode fiber (PANDA).

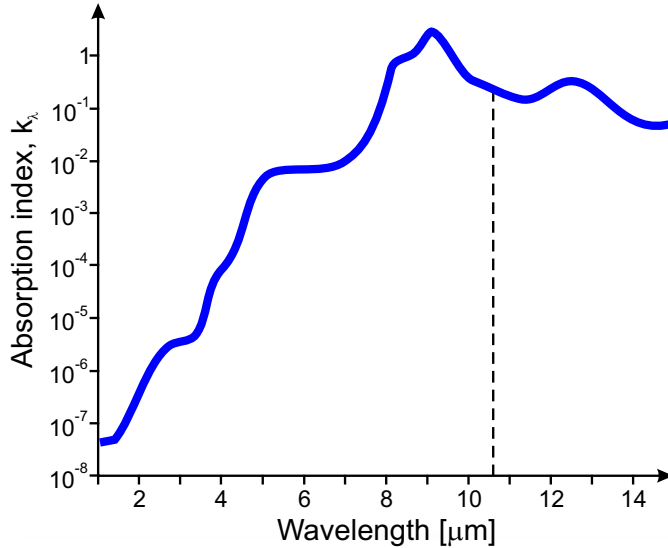


Figure 2.5: The absorption index of fused silica for wavelengths between 1 and 15 μm . Therefore, the CO_2 at 10.6 μm is suitable to fabricate a fiber mirror. Sketch from [15].

2.2 Fiber mirror

The CO_2 laser emerged as a very successful tool to fabricate a concave profile on a fiber end facet, since at the laser transition of 10.6 μm strong absorption is observed for fused silica glass as shown in Fig. 2.5. The sudden heating of the fused silica by a focused beam with an intensity of around 100 W/mm^2 has two effects. On one hand material is evaporated from the surface which defines the structure on the fiber end facet and on the other hand the surface is smoothed by melting of a surface layer of a few μm . The CO_2 laser and the ablation process to fabricate the fiber mirrors is subject of this chapter.

2.2.1 CO_2 laser

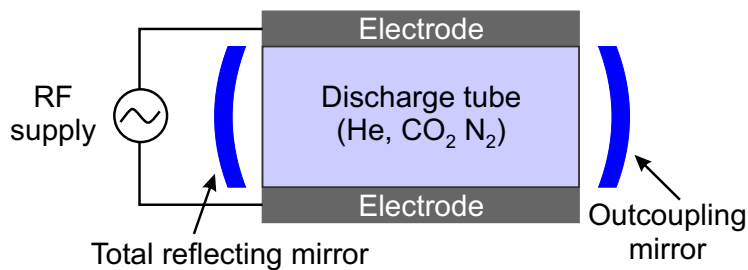


Figure 2.6: A CO_2 laser consists of a sealed discharge tube of a gas mixture containing CO_2 , N_2 and He with a ratio of about 10:15:75. An electrical field between two electrodes is applied, energetic electrons brings the ground state of N_2 into the excited state and by collisions with the N_2 molecules the CO_2 molecules are pumped into the excited state.

The CO_2 laser¹ consists of a sealed discharge tube of a gas mixture containing CO_2 , N_2 and He with a ratio of about 10:15:75 as sketched in Fig. 2.6. For an efficient laser operation the maintenance of a low gas temperature at room temperature is necessary. For the fabrication of fiber mirrors an optical power of about 1 W is used and the thermal heat is sufficiently convected

¹FIRESTAR v20 and v30, SYNRAD

out of the laser cavity by wall cooling. The helium serves as a coolant for the CO₂ molecules because of a good heat conductance and the temperature is stabilized by water cooling of the laser. The profile of the laser beam has a large effect on the fabricated structure. Therefore, a Gaussian beam with an radial intensity distribution $I(r)$ with a beam radius w_r is used:

$$I(r) = I_0 e^{\frac{-2r^2}{w_r^2}}. \quad (2.2)$$

2.2.2 Ablation process

The CO₂ laser is most suitable to create an almost gaussian shaped structure with a low surface roughness down to 2 nm rms due to the right balance between ablated material and melting [16]. Both mechanisms will be discussed theoretically in this chapter. Furthermore different profiles can be fabricated by varying the CO₂ laser power, the beam radius and the illumination time of the fiber end facet.

Evaporation

To understand the evaporation and melting effect, the temperature profile has to be examined. It is analytically determined from the two dimensional heat conduction equation of a two-dimensional problem under the assumption of a ideal gaussian laser beam profile with the power P and the beam radius w_r and an unlimited surface. The temperature distribution depends on the properties of fused silica namely the absorption A , the thermal conductivity κ and the thermal diffusivity D . If the sample is illuminated for a time τ , the temperature profile is given by [17]:

$$T(r, \tau) = \frac{AP}{2\kappa} \sqrt{\frac{D}{\pi^3}} \int_0^\tau \exp\left(\frac{-r^2}{\frac{w_r^2}{2} + 4Dt}\right) \left(\sqrt{t} \frac{w_r}{2} + 4Dt\right)^{-1} dt. \quad (2.3)$$

Since only the central region of the profile serves as the mirror, this region can be approximated by a parabolic temperature distribution. Furthermore, a rectangular laser pulse in the millisecond regime is assumed due to small rise and fall times of the laser in the order of microseconds. In our case we have beam intensities of about 10 kW/cm² [17] where the main cooling mechanism is lateral heat transport and evaporation cooling can be neglected. Therefore, the velocity of the evaporation front defines the structure after the illumination time τ . The depth of the profile $z(r)$ is then given depending on the temperature in the center of the spot $T(0, \tau)$ by [17]:

$$z(r) = z_0 \exp\left(-\frac{U}{k_B T(0, \tau)} \frac{r^2}{2w_r^2}\right), \quad (2.4)$$

$$T(0, \tau) = \frac{AP}{\sqrt{2\pi^3} w_r \kappa} \arctan\left(\frac{2D}{w_r^2} \tau\right). \quad (2.5)$$

The latent heat of evaporation for fused silica U is given by 3.6 eV and z_0 is the total depth of the structure. In the equation 2.4 and 2.5, one can see, that the profile depends on the CO₂

laser beam power, the beam radius and the illumination time. These three ablation parameters are varied to fabricate different fiber mirrors. The $1/e^2$ diameter d is then given by [17]:

$$d \approx 2w_r \sqrt{\frac{k_B T(0, \tau)}{U}}. \quad (2.6)$$

The profile is completely determined by two parameters the depth $z(r)$ and the distance r to the center of the structure. The most important parameter is the radius of curvature R of the profile in the central mirror region with r defined in an interval about $[-10, 10] \mu\text{m}$ [16]. A circular segment can be approximated to the region of interest in the case that $z(r) = z_r \ll r$ as shown in figure 2.7:

$$R = \frac{r^2}{2z_r} + \frac{z_r}{2} \approx \frac{r^2}{8z_r}. \quad (2.7)$$

With $A = 0.85$, $\kappa = 1.38 \text{ W/mK}$ and $D = 7.5 \times 10^{-9} \text{ m}^2/\text{s}$ at room temperature this description

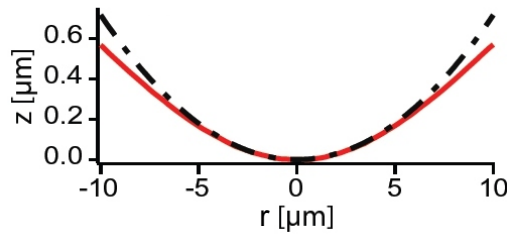


Figure 2.7: The center of the Gaussian profile on the fiber end facet with the depth z (red solid line) in the distance r from the center can be approximated with a circular segment (black dashed line) in this particular case with $R = 70 \mu\text{m}$ [11].

suits very well for the structures on a fused silica plate [18]. On the fiber with a limited surface however, the temperature can not propagate in the same way as assumed in the analytical solution for an unlimited surface and the results deviates from the theory [16]. Nevertheless the dependency between the structures and the three parameters, namely the beam power, the beam radius and the illumination time is observed and therefore these parameters are used to fabricate different structures.

Melting

For a temperature over $2000 \text{ }^\circ\text{C}$ [17], the viscosity of fused silica decreases significantly such that a layer of a few micrometer melts as shown in Fig. 2.8. The thickness is defined between the surface and the layer with a viscosity ten times larger than at the surface. The melting depends also on the CO_2 laser power, the beam radius and the laser pulse duration. The parameters have to be carefully chosen such, that the backflow of the material does not become too large and contracts to a convex structure due to surface tension in the central region of the profile or at the surrounding of the structure since the fiber surface is limited. For the fiber mirror fabrication the task is to smooth out irregularities of the surface. Measurements with an atomic force microscope show, that surface roughnesses down to $\sigma < 0.2 \text{ nm rms}$ are achieved [16].

2.3 Fiber Fabry-Pérot cavity

The assembled fiber cavity in Paris, which is described in chapter 5 supports the fundamental TEM_{00} mode and consists of two mirrors fabricated on a singlemode and multimode fiber. It

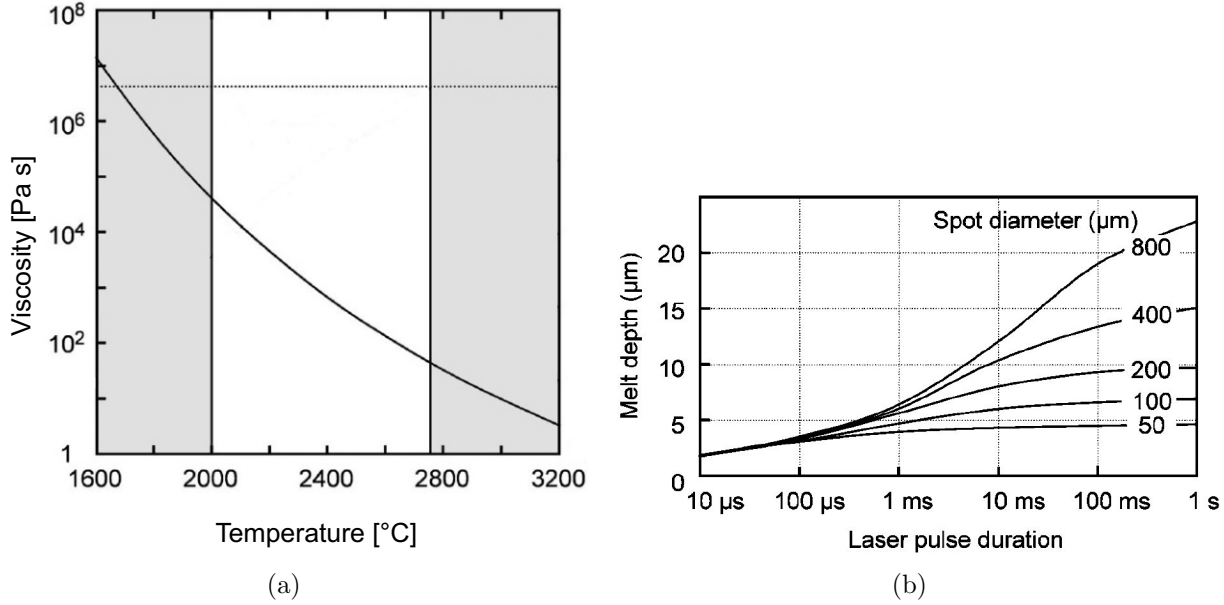


Figure 2.8: Melting: For a temperature over 2000 °C the viscosity (a) of fused silica decreases significantly such that a layer of a few micrometer melts (b). The calculated melt depth depends on the laser pulse duration for different laser beam diameter $2w_r$. The thickness is defined between the surface and the layer with a viscosity ten times larger than at the surface [19].

is common to use a singlemode fiber for the incoupling because then only one mode is coupled into the cavity. For an efficient light collection the light is coupled out with a multimode fiber since the mode matching doesn't need to be optimized as it would be the case for a singlemode-singlemode cavity. The topic of this chapter is the description of the fundamental TEM_{00} cavity mode and which boundary conditions have to be fulfilled. Furthermore, the characteristics of the cavity itself and the optical properties of the mode field inside the cavity are discussed. The derivation follows mainly [20].

2.3.1 Gaussian beams and the TEM_{00} mode

Propagating laser beams as well as mode fields inside of a cavity can be described with Gaussian optics. The transverse profile of the fundamental TEM_{00} mode is described by the complex scalar wave amplitude $E(x, y, z)$ in free space. In Cartesian coordinates the Maxwell equation reduces by using the paraxial wave approximation to

$$\left(\frac{\partial^2}{\partial x^2} + \frac{\partial^2}{\partial y^2} - 2ik \frac{\partial}{\partial z} \right) E = 0, \quad (2.8)$$

where $k = 2\pi/\lambda$ denotes the wave number and the beam propagates along the z axis. The solution with $r^2 = x^2 + y^2$ is then given by:

$$E(r, z) = E_0 \cdot \exp\left(-\frac{r^2}{w_r^2(z)}\right) \cdot \exp\left(-ik \frac{r^2}{2R^2(z)}\right) \cdot \exp(-ip(z)). \quad (2.9)$$

In this equation $p(z)$ denotes the Gouy phase shift, $R(z)$ the radius of curvature at any plane and $w_r(z)$ the spot size depending on the Raleigh length z_0 :

$$w_r(z) = w_0 \sqrt{1 + \left(\frac{z}{z_0}\right)^2}, \quad (2.10)$$

$$z_0 = \frac{\pi w_0^2}{\lambda}. \quad (2.11)$$

The transverse radial intensity distribution of the gaussian beam with a radius w_r and the maximum intensity I_0 is then given by:

$$I(r) = I_0 \exp\left(-\frac{2r^2}{w_r^2}\right). \quad (2.12)$$

2.3.2 Properties of the optical cavity

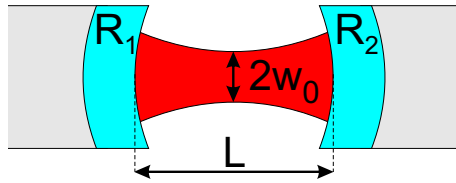


Figure 2.9: Scheme of a cavity with radii of curvature R_1 , R_2 and the cavity length L confining a light field with a mode waist w_0 .

Three geometrical properties of the cavity specify the mode applied in the cavity as sketched in Fig. 2.9: The wavefront curvature $R(z)$ of the gaussian beam must match the radii of curvature R_1 and R_2 at each mirror with respect to the cavity length L . The mode waist w_0 of the cavity mode is then given by:

$$w_0^2 = \frac{L\lambda}{\pi} \sqrt{\frac{g_1 g_2 (1 - g_1 g_2)}{(g_1 + g_2 - 2g_1 g_2)^2}}, \quad (2.13)$$

$$\text{with } g_i = 1 - \frac{L}{R_i}, \quad i = 1, 2. \quad (2.14)$$

The mode volume V_{mode} of the light field is an important parameter since it influences the interaction between the mode field and atoms in the cavity. For the fundamental TEM_{00} mode the mode volume can be approximated to [10]:

$$V_{\text{mode}} = \frac{\pi}{4} w_0^2 L. \quad (2.15)$$

The cavity only forms a stable periodic focusing system when the beam doesn't leave the system in the transversal direction. The stability range is then confined by [21]:

$$0 \leq g_1 g_2 \leq 1. \quad (2.16)$$

Here it is assumed, that the transverse size of the mirror is larger than the size of the beam at the mirror surface. The stability diagram (Fig. 2.10) shows when a unique set of gaussian transverse resonator modes is supported.

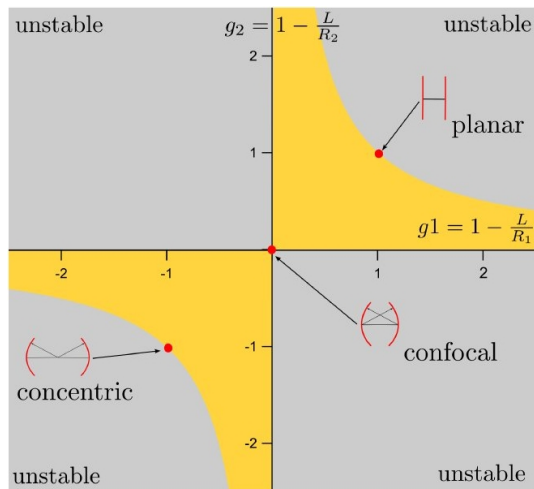


Figure 2.10: The stability diagram of an optical cavity with spherical mirrors depends on the radii of curvature R_1 , R_2 and the cavity length L . The yellow region indicates a stable periodic system when the beam doesn't leave the lens system. The symmetric planar, confocal and concentric cavities are examples of a metastable geometry. Sketch from [16].

2.3.3 Cavity spectrum

A transmission signal like sketched in Fig. 2.11 is typical for a Fabry-Pérot cavity with the refractive index n of the medium inside the cavity and a cavity length L . Here the transmitted power is shown as a function of the frequency. A resonance peak is observed if the following condition is fulfilled:

$$L = m \frac{\lambda}{2n} \quad \text{for} \quad m = 1, 2, \dots \quad (2.17)$$

The interferometer is characterized by two quantities of the transmission signal. The free spectral range (FSR) and the full width half maximum (FWHM) of the resonance peak. The free spectral range in the frequency and wavelength domain is defined as the distance between two resonance peaks:

$$\Delta\nu_{\text{FSR}} = \frac{c_0}{2nL} \quad \text{and} \quad \Delta\lambda_{\text{FSR}} = \frac{\lambda^2}{2nL}. \quad (2.18)$$

Obviously the resonance peaks are only equidistant on the frequency scale. But for wavelength which are high compared to the free spectral range $\Delta\lambda_{\text{FSR}}$, however, the distance stays approx-

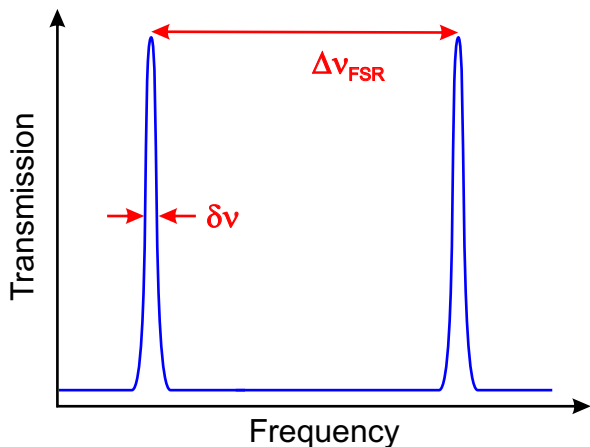


Figure 2.11: The scheme shows the transmitted power of a Fabry-Pérot cavity. The transmission signal can be characterized by two quantities: the full width half maximum of the resonance $\delta\nu$ and the free spectral range $\Delta\nu_{\text{FSR}}$.

imately constant also for the wavelength scale. With the FWHM of the resonance peak in the frequency domain $\delta\nu$ the finesse \mathcal{F} of the cavity is defined by:

$$\mathcal{F} = \frac{\Delta\nu_{\text{FSR}}}{\delta\nu}. \quad (2.19)$$

A picturesque description of this quantity is that a photon makes \mathcal{F}/π round trips on average before it leaves the cavity. The finesse increases for larger mirror reflectivities and can be expressed as follows when the losses like scattering and absorption can be neglected and we assume two identical mirror reflectivities $R_{\mathcal{F}} = R_1 = R_2$:

$$\mathcal{F} \approx \frac{\pi\sqrt{R_{\mathcal{F}}}}{1 - R_{\mathcal{F}}}. \quad (2.20)$$

The cavity decay rate $\kappa = \frac{\delta\nu}{2}$ of the cavity is connected to the finesse and the free spectral range:

$$\kappa = \pi \frac{\Delta\nu_{\text{FSR}}}{\mathcal{F}}. \quad (2.21)$$

In this thesis I investigate also a further special parameter namely the resonance splitting. Intrinsic stress in the mirror coating induces birefringence. This effect occurs in most materials and is usually so small, that it is negligible. In this case, however, this effect leads to two linearly polarized orthogonal modes with a frequency difference in the megahertz regime. The optical path in the coating is polarisation dependant and the splitting depends on the cavity length L :

$$\nu_{\text{split}} = \frac{c\delta_{\text{split}}}{4\pi L}. \quad (2.22)$$

Here δ_{split} is the phase shift between the two modes a and b after one round trip:

$$\delta_{\text{split}} = \delta_b - \delta_a, \quad (2.23)$$

$$\text{where } \delta_i = k_i z = 4\pi L \frac{1}{\lambda_i}, \quad i = a, b. \quad (2.24)$$

The ordinary and extraordinary axis of the two mirrors are independent to each other. By the rotation of one fiber mirror around the cavity axis, the optical path in the coating changes for the two modes. This is sketched in Fig. 2.12 for two identical fiber mirrors with the refractive indices n_0 and n_e . In the first case the ordinary and extraordinary axes are parallel to each other and the wavelength difference between both modes is maximal. If the axes are not parallel to each other both modes have an effective refractive index, which is a linear combination of n_0 and n_e . In the other extreme case for this cavity, the axes are perpendicular to each other and the wavelength of both modes is equal. The resonances overlap completely. For a real cavity the refractive indices n_0 and n_e are different for both cavities.

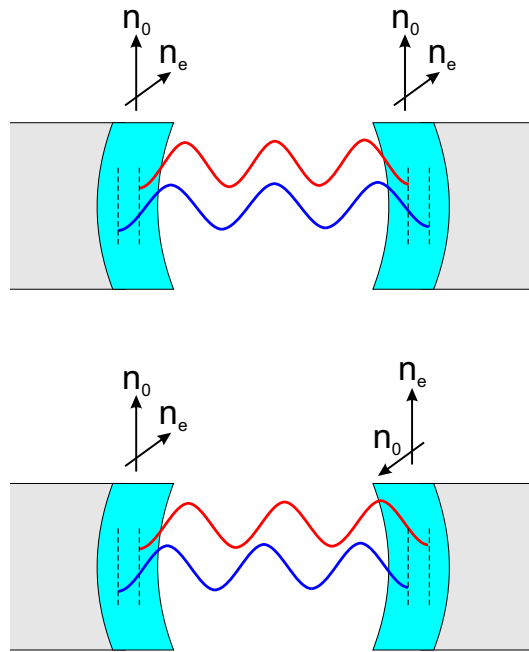


Figure 2.12: Resonance splitting: Intrinsic stress in the mirror coating induces birefringence. In the cavity this effect leads to two linearly polarized orthogonal modes in red and blue with a frequency difference in the megahertz regime. The different optical paths in the coating are implied as a different penetration depths. For a cavity made of two identical fiber mirrors with the refractive indices n_0 and n_e the wavelength difference between both modes is maximal if the ordinary and extraordinary axes are parallel to each other as shown in the first case. In the other extreme case, the axes are perpendicular to each other and the wavelength of both modes is equal.

3 Fabrication of fiber mirrors in Paris

The first fiber mirrors were fabricated with the CO₂ ablation setup in Paris [16]. In this chapter I will first describe the setup and its operation. Then I will discuss some enhancements to the setup which include the adjustment of the ablation parameters, the improvement of the CO₂ laser beam and an investigation of the reproducibility of the ablation process. Furthermore, I will describe the characterisation of the mirror structure with a profilometer. Finally the fabrication process includes also the addition of a highly reflective dielectric coating.

3.1 Fiber preparation

Before a structure is fabricated on a fiber end facet, the fiber has to be prepared. The coating is removed at the fiber end facet. For an acrylate jacket, the coating can be stripped. The copper coating can be etched away by an iron(III) chloride aqueous solution and the fiber is cleaned thoroughly with distilled water afterwards. In both cases the bare fiber is finally cleaned with isopropanol or methanol and cleaved to receive a plane end facet.

3.2 CO₂ laser

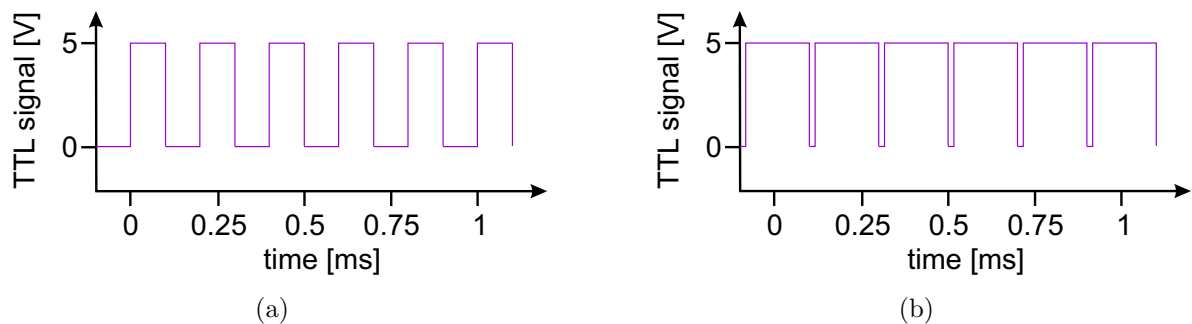


Figure 3.1: Pulsed pumping of the CO₂ laser: The TTL pumping signal is adjusted via the pulse-width modulation (PWM) frequency and the duty cycle (DC). (a) shows a signal with PWM = 5 kHz and DC = 0.5 and (b) with PWM = 5 kHz and DC = 0.95.

The CO₂ laser² is operated in the pulsed pumping mode which is sketched in Fig. 3.1. The TTL pumping signal is set³ by the pulse-width modulation (PWM) frequency and the duty cycle (DC). If the time interval between the pulses is on the same order of magnitudes as the rise and fall times of $\tau_r = 50 \mu\text{s}$ and $\tau_f = 100 \mu\text{s}$, the laser operates in a quasi CW mode.

Even though only a laser power of about 1 W is required to fabricate a concave structure with the desired parameters, this 20 W laser is used, because it provides a long time power stability. This is necessary, since the structure $z(r)$ is sensitive to the laser power P as shown in Eq. (2.4) and (2.5). A precise power measurement in Fig. 3.2 shows, that the power fluctuations reduces after a heat-up phase of 15 minutes to 0.1% which enables reproducible processes. The power

²FIRESTAR v20 (water cooled), SYNRAD

³UC-2000 LASER CONTROLLER, SYNRAD

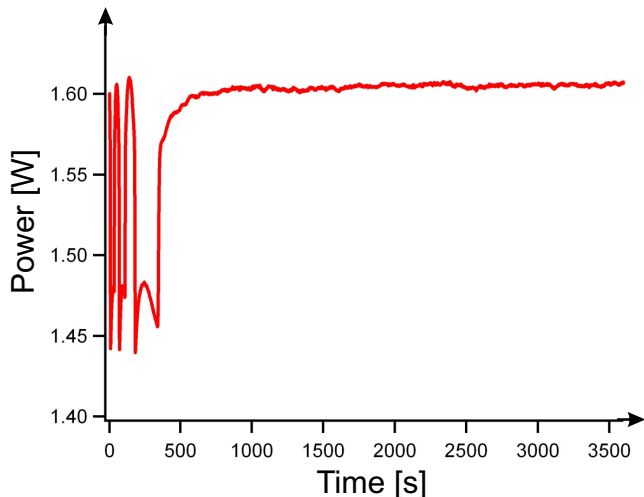


Figure 3.2: Power measurement of the CO₂ laser: The measured output power shows the heat-up phase with power fluctuations about 10%. After 15 minutes the fluctuations reduces to about 0.1% which enables reproducible processes: $P = 1.605 \pm 0.001$ W, PWM = 5 kHz, DC = 0.08. Taken from [16].

fluctuations of about 10% after switching on the laser occur because of frequent mode jumps during the thermalisation processes in the laser. At the output of the CO₂ laser the beam has a diameter of about 2.5 mm and a divergence of about 3.5 mrad. The mode quality $M^2 < 1.1$ enables to fabricate circular structures on a fiber end facet.

3.3 Ablation setup

The ablation setup is sketched in Fig. 3.3. The cleaned and cleaved fiber is fixed by two to three elastomer covered magnetic clamps into a V-groove on a XYZ positioning stage with nanometer precision⁴. The CO₂ laser beam is first expanded by a Keplerian telescope with a magnification of about 1.6. The two lenses⁵ are mounted on an optical rail. In this way the lenses can be shifted along the rail without loosing the general alignment for the CO₂ laser beam. The beam is then focused onto the fiber end facet with a third lens. With the beam expansion by the telescope, small beam waists down to 30 μ m are achieved behind the focusing third lens.

During the ablation process on silica plates it was observed that about 15% of the IR radiation is reflected back into the laser. This leads to frequent mode jumps resulting in power fluctuations. Therefore, an isolator is implemented into the setup. It consists of a $\lambda/4$ plate and a wire grid polarizer which are installed behind the telescope. This yields an attenuation of the power fluctuation of 9.5 dB [16].

For the alignment of the optical elements in the setup, one can use alignment paper or the HeNe laser alignment pointer, the CO₂ laser is equipped with. This laser pointer in the visible spectrum is overlapped with the CO₂ laser beam. The HeNe laser beam is mostly blocked by the isolator and can not be used for an optical alignment of the fiber in the CO₂ laser beam.

The fiber is monitored with a microscope which consists of an objective lens⁶ with a large

⁴NANOMAX 313, THORLABS GmbH

⁵All lenses are made of ZnSe, ULO OPTICS

⁶M PLAN APO 10x, MITUTOYO

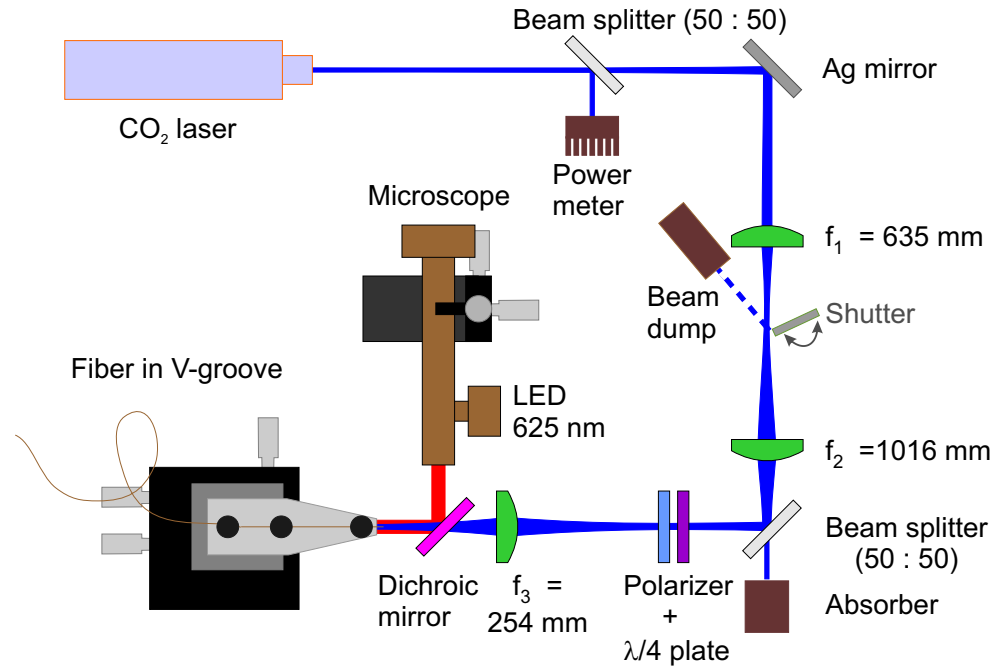


Figure 3.3: CO₂ ablation setup in Paris.

working distance $d_{\text{work}} > 30$ mm and a 12x UltraZoom lens. It is completed with a CCD camera⁷ and mounted on a XYZ stage⁸. The implementation of the microscope into the setup is realized by an dichroic mirror⁹ (DM) between the fiber and the third lens. The DM is transparent for the CO₂ laser light and reflective for visible light with a maximum reflectivity at 630 nm. The light source of the microscope radiates at $\lambda = 625$ nm. With the microscope one can determine, whether the preparation of the fiber or the ablation process were successful. In addition it is used for an optical positioning of the fiber which is explained later in this chapter.

Ablation sequence

The fiber is illuminated by the CO₂ laser beam for some milliseconds. The duration varies between 5–300 ms. By just switching the laser on and off, power fluctuations similar to those in the heat-up phase would occur. Since the profile $z(r)$ is proportional to $z_0(P)\exp(1/P)$, the reproducibility of the mirrors is enhanced by using a shutter. In this case the shutter deflects the laser beam into a beam dump. In this way the laser can be operated in the quasi CW mode until it stays in thermal equilibrium after the heating period. The shutter is a silver mirror mounted on a computer controlled electromechanical switch. It is placed in the focal point between the two telescope lenses, because at that position the time to open and close the shutter is minimized. The shutter is opened for some milliseconds to illuminate the fiber end facet with low power fluctuations.

⁷DP300, DELTAPIX

⁸M UMR 8.25, NEWPORT

⁹ULO OPTICS

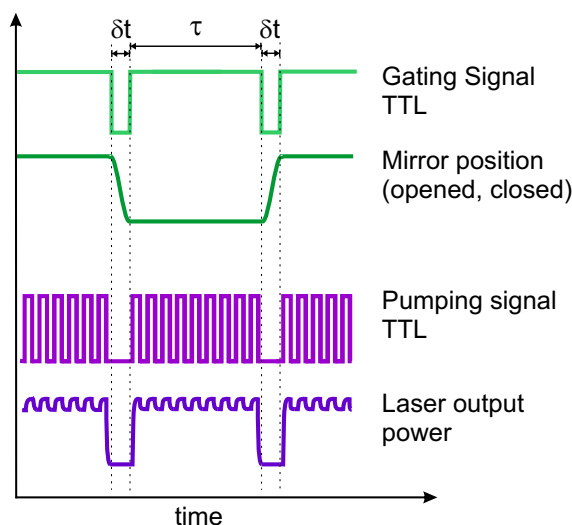


Figure 3.4: Sequence during an ablation process: The green signals show the gating signal and the mirror position of the shutter. δt describes the transit time and τ corresponds to the length of the CO_2 laser pulse. In purple the pumping signal of the CO_2 laser and its output signal is shown. In this way thermalisation processes in the laser are reduced and the shutter does not chop the beam during the transit.

Since the time of the shutter is in the same order of magnitude as the illumination time, the shutter would chop the beam. This would lead to an asymmetric illumination of the fiber and in consequence an asymmetric mirror profile. To circumvent this we take advantage of the short rise and fall times of the CO_2 laser of about 100–150 μs .

The ablation sequence is sketched in Fig. 3.4. At the beginning the shutter is closed. Then the laser is switched off and the shutter is opened in about $\delta t = 20$ ms. Afterwards the laser is switched on again for the time τ and is switched off again. Finally the shutter is closed and the laser is switched back on. Doing so, we can approach a rectangular illumination pulse which enables an analytical approach of the ablation process described in chapter 2.2.2.

Optical adjustment of the fiber

The CCD camera of the microscope is connected to a computer. On one hand the microscope is used to analyse roughly the fiber surface before and after the ablation process. Before the shooting the surface quality is judged concerning a clean cleave as well as a contaminated surface and after the shooting the centering as well as the shape of the profile is evaluated. To use the microscope for the visual alignment of the fiber end facet, the following alignment is done: First the position of the laser beam has to be located with the microscope. Since a common object slide has a much larger plane surface than a cleaved fiber, it is used for this alignment and mounted on the XYZ positioning stage of the fiber. Then structures are fabricated with a CO_2 laser power around 2 W. Around the focal point a flash is observed during the ablation process with a maximal brightness in the focal point. To facilitate the locating of the structure with the microscope, the border of the object slide is struck to get a point of reference.

In a second step the right position in beam direction is adjusted. Therefore, the object slide is shifted in z-direction in 200 μm steps for a rough alignment and each time a structure is fabricated as shown in Fig. 3.5. One can also see in this figure, that most of the structures are elliptically shaped because the CO_2 laser beam is astigmatic in the focal point. Astigmatism means here that the vertical waist is not at the same position as the horizontal waist. The mirror profiles, however, should be circular shaped, to avoid an additional degree of freedom. That means for a fixed constellation of the three lenses in the ablation setup, there is only one

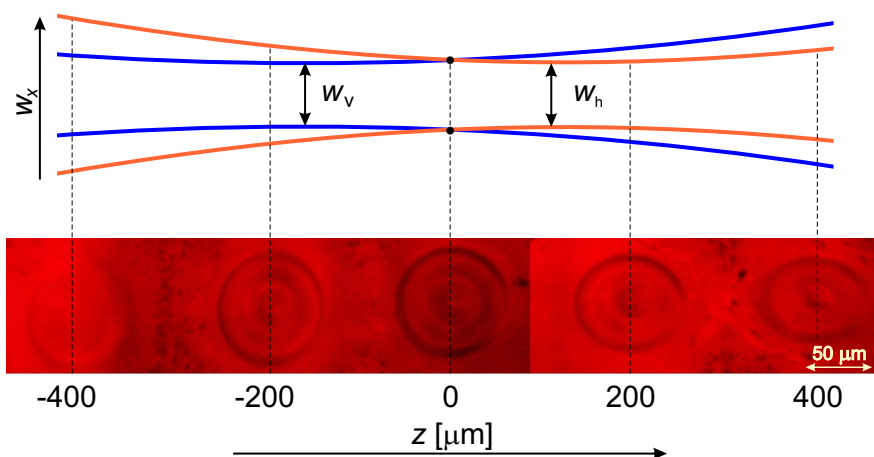


Figure 3.5: In the upper image the astigmatic laser beam is sketched for the vertical and horizontal plane with the $1/e^2$ waists w_v and w_h . Structures were fabricated on an object slide with a CO_2 beam radius $w_r = 38 \mu\text{m}$ at, $P = 1.6 \text{ W}$ around the focal point in 200 nm steps, which is shown in the lower image. The elliptical shape of the structures indicates the astigmatism. In the center of the structures a convex shape is visible which comes from the backflow of the melted material towards the center during the ablation process due to surface tension. Only the position with two equal beam waists is used for the mirror fabrication.

useful position between the two waists to fabricate a fiber mirror. This position is precisely determined next in $10\text{--}20 \mu\text{m}$ steps. Finally the transversal position of the structure center is marked on the computer screen and the microscope is aligned with an precision of about $7 \mu\text{m}$ due to the depth of field of the microscope and a fiber can be positioned [16].

3.4 Ablation parameter

The three ablation parameter are the CO_2 laser power P , the beam radius w_r and the illumination time τ as explained in chapter 2.2.2. The power is changed by the duty cycle as shown in Fig. 3.1 and the illumination time by the pumping and gating signal of the laser and the shutter as shown in Fig. 3.4. Due to the astigmatic laser beam, the CO_2 laser beam size is changed as follows:

By changing the distance d_1 between the two lenses of the Keplerian telescope, the waist w_0 changes after the third lens as it is shown in Fig. 3.6. The dependency is measured in the

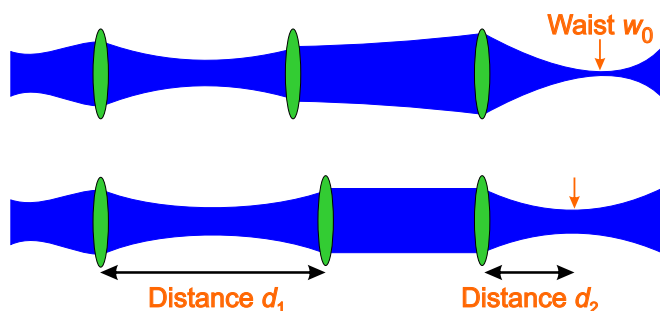


Figure 3.6: Sketch of the CO_2 beam passing the three lenses of the setup: By varying the position of the second telescope lens, the waist of the CO_2 laser beam and its position changes behind the third lens.

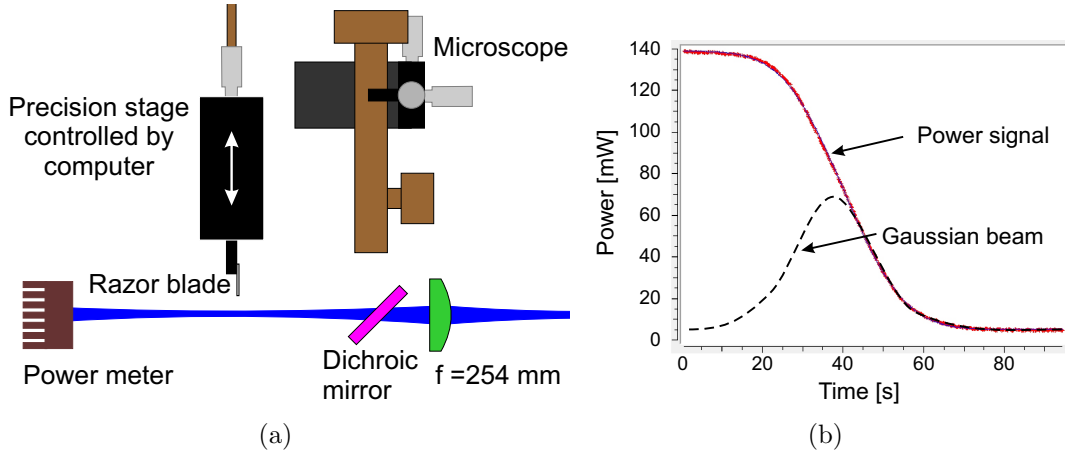


Figure 3.7: Measurement of the beam waist of the CO₂ laser with the knife edge method: (a) A razor blade is driven into the beam with a computer controlled stage in x-direction. From the power signal behind the razor blade in (b) the beam radius can be extracted. The behavior of the power signal depends directly from the width of the intensity profile of the Gaussian beam which is indicated in the same figure.

following. Therefore, the waist of the CO₂ laser is determined with the knife edge method shown in Fig. 3.7(a). A razor blade is driven with a constant velocity into the beam with a computer controlled stage in x-direction. During this process the laser power behind the razor blade is measured as shown in Fig. 3.7(b):

$$\begin{aligned}
 P(x) &= P_{\text{TOT}} - I_0 \int_{-\infty}^x e^{-\frac{2x'^2}{w_x^2}} dx' \int_{-\infty}^{\infty} e^{-\frac{2y^2}{w_y^2}} dy \\
 &= \frac{P_{\text{TOT}}}{2} \left[1 - \operatorname{erf} \left(\frac{\sqrt{2}x}{w_x} \right) \right].
 \end{aligned} \tag{3.1}$$

P_{TOT} is the total power of the beam. For the determination an ideal Gaussian shaped CO₂ laser beam is assumed. In the xy -plane it has the following intensity with a peak intensity I_0 and $1/e^2$ radii w_x, w_y :

$$I(x, y) = I_0 \exp \left(-\frac{2x^2}{w_x^2} - \frac{2y^2}{w_y^2} \right). \tag{3.2}$$

By fitting an error function to the power signal, the beam radius w_x is obtained. This procedure is repeated at different z positions around the focal point. With these informations the beam profile is fitted in z -direction $w_x(z)$ with the Rayleigh length z_0 , the distance d_2 and the beam waist w_0 as the fit parameters between the focusing lens and the the focal point as shown in Fig. 3.8:

$$w_x(z) = w_0 \sqrt{1 + \left(\frac{z - d_2}{z_0} \right)^2}. \tag{3.3}$$

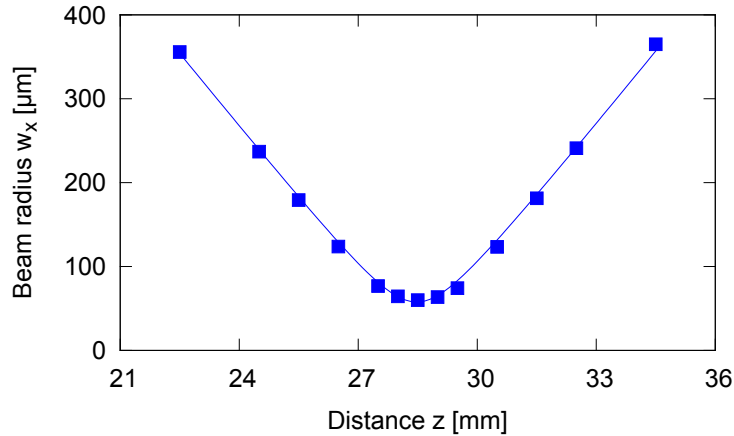


Figure 3.8: Determination of the CO₂ beam waist by fitting the beam profile in beam direction $w_x(z)$ to the data of the knife edge method: $w_0 = (58 \pm 4) \mu\text{m}$.

This measurement is repeated for different distances d_1 between the two telescope lenses. In Fig. 3.9 the dependency is shown as well as the change of the position of the waist along the beam direction. The uncertainty for the distance between the telescope lenses is estimated with

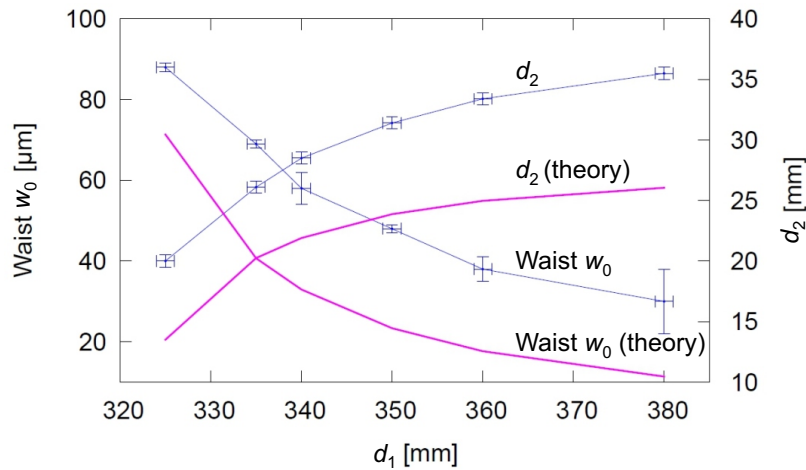


Figure 3.9: Dependency of the waist and its position d_2 behind the third lens from the distance d_1 between the two telescope lenses. With this ablation setup waists of 30–90 μm are achieved. For the theoretical examination the dichroic mirror (DM) is not considered. Since the DM causes large aberrations as discussed in chapter 3.6 the beam cannot be assumed as an ideal Gaussian beam anymore and this explains the significant deviation to the measured data.

$\Delta d_1 = 1 \text{ cm}$ and for the distance between the third lens and the focal point by $\Delta d_2 = 0.5 \text{ mm}$. The uncertainty for the waist comes from the fitting of Eq. (3.3) to the data.

Discussion

With the ablation setup in this configuration waists of 30–90 μm are achieved. The course of the waist and the waist position for an increasing distance of the telescope lenses is as expected. The waist increases while the position of the waist approaches to the third lens. For the waist of 30 μm the waist position comes so close to the dichroic mirror that it is not measurable further with this setup. For a waist of 90 μm the distance between the two telescope lenses is maximal until the next optical element is reached. A significant deviation between the measured data and the calculated values is observed. For the calculation an ideal Gaussian beam is considered and the dichroic mirror is neglected. As it will be discussed in chapter 3.6, the dichroic mirror

causes large aberrations and the beam cannot be assumed as an ideal Gaussian beam anymore. In Fig. 3.16 the influence of the tilted dichroic mirror in the focused beam is simulated. The beam waist is larger with the dichroic mirror which is also observed in Fig. 3.9. Moreover, it is noticeable, that the error for smaller waists increases. This might also come from the astigmatic property of the laser beam. The effect is larger for a strong focused beam and the beam deviates more from a Gaussian shape. The fitting of an ideal Gaussian beam to the data leads to a larger fit error.

To get even larger or smaller waists the ablation setup can be configured by changing the position of the lenses or by exchanging the third lens by a lens with a different focal length.

3.5 Characterisation of the profile on the fiber end facet

The topography of the profile is determined with two different methods: an atomic force microscope (AFM) and a white light interferometer. The measurement with an AFM is very precise and includes the information of the surface roughness, but it is also very time consuming compared to the second method. The white light interferometer is a good and fast approach and satisfies the requirements to determine the topography.

Two different profilometers are compared, the Mirau and the Fizeau profilometer, which are both non-contact interferometers. The basic principle is the same. A high power LED is used as a light source. A beamsplitter splits one part of the light to be focused onto the probe and the other part to be focused onto a plane reference surface. The backreflected light is recombined and interferes, which is observed with a CCD camera. In this way the surface is illuminated uniformly and due to the limited coherence length only the picture of fiber end facet and a reference surface interfere.

3.5.1 Mirau profilometer

The Mirau profilometer and a detailed view of the Mirau objective is shown in Fig. 3.10. The light source is a 505 nm high power LED¹⁰. The light source is not directly placed in the focal point of the following lens, because then the image of the light source is simultaneously visible with the interference pattern which disturbs an optical evaluation of the interferogram. The aperture in front of the light source reduces aberrations which increases the contrast of the interference fringes. After the beamsplitter the light passes the Mirau objective¹¹. This objective contains a further beamsplitter. One part of the light is transmitted and focused onto the fiber end facet and the other part is reflected and focused on a small plane reference mirror. The backreflected light from the mirror and the light from the probe are recombined by the same beamsplitter and then observed with a CCD camera¹². The interferogram of a processed fiber with a diameter of 125 μm is shown in the same figure.

To observe the interference pattern the optical path length difference between the two backre-

¹⁰THORLABS M505L2

¹¹NIKON 20x NT 59-313

¹²THORLABS DCC1645C

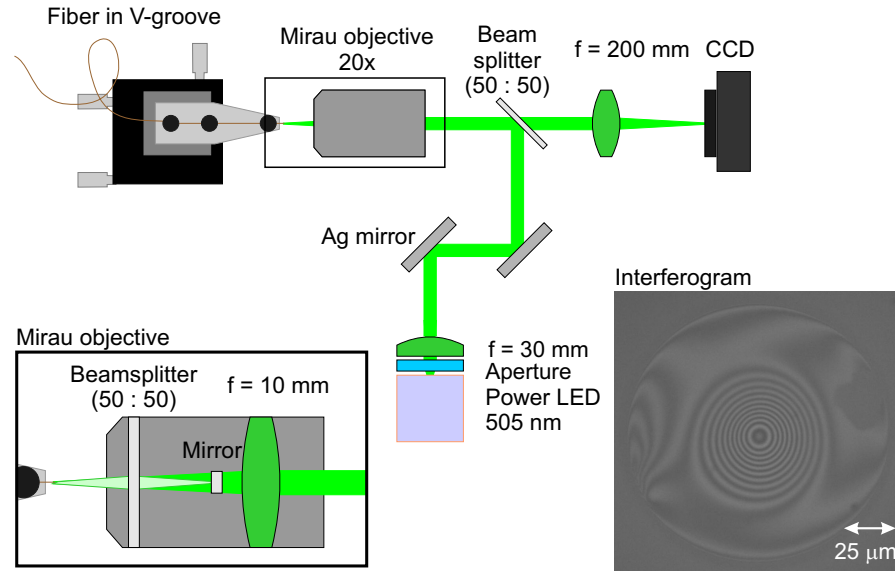


Figure 3.10: Mirau profilometer: The setup and a detailed view of the Mirau objective are shown. The backreflected beam from the fiber surface and from the reference mirror inside the objective interfere which is observed with a CCD camera. From the obtained interferogram of a fiber the radii of curvature $R_h = (65 \pm 3) \mu\text{m}$, $R_v = (68 \pm 3) \mu\text{m}$ in horizontal and vertical direction as well as the profile are determined.

flected beams need to be smaller than the coherence length l_c :

$$l_c = \frac{\lambda^2}{\Delta\lambda} = 9 \mu\text{m}. \quad (3.4)$$

The spectral width $\Delta\lambda$ for this light source is 30 nm. Since the distance between the beamsplitter of the Mirau objective and the mirror is fixed, the lens in front of the CCD camera has to be aligned such that the pictures from the probe and from the reference are spatially overlapped within half the coherence length. Therefore, the interference pattern is also observed only for a structure depth specified by half the coherence length.

The fiber is mounted in a V-groove on a XYZ nanometer positioning stage. Since the two surfaces need to be parallel to each other for the spatial overlap in the transversal plane two goniometers are added to the XYZ stage to correct the two angular degrees of freedom.

3.5.2 Fizeau Profilometer

This profilometer is implemented in the ablation setup and based on Newton rings. As shown in Fig. 3.11 a high power LED with a wavelength of $\lambda = 625 \text{ nm}$ and a bandwidth of 20 nm is used as a light source which is implemented in the microscope. A bandpass filter of 3 nm increases the coherence length to $l_c = 130 \mu\text{m}$. A common object slide serves as a beam splitter. A part of the light is backreflected from the plane back side of the object slide which serves as the reference and the other part is transmitted. The interference pattern is observed with the microscope of the ablation setup. To correct the angle of the surface from the object slide with respect to the fiber surface the stage is equipped with a goniometer. The light backreflected

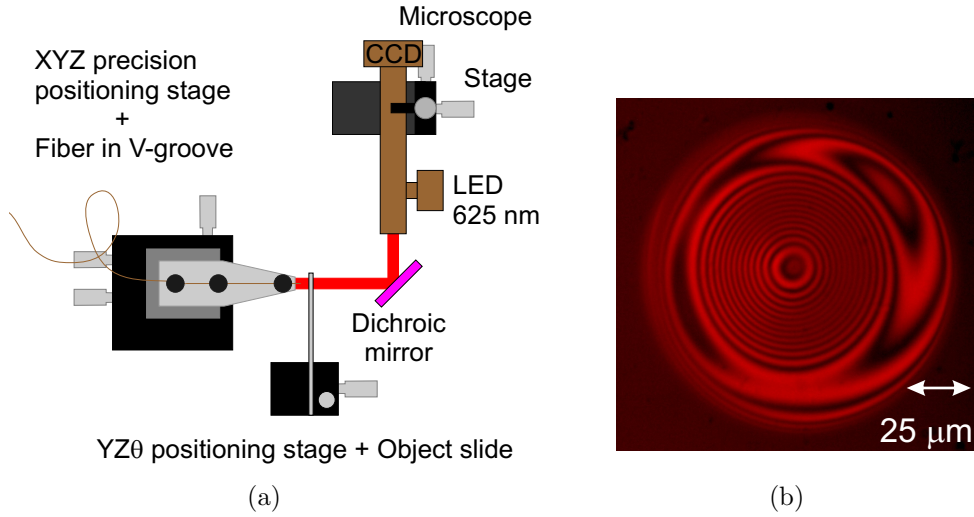


Figure 3.11: Fizeau profilometer: (a) shows the setup within the CO_2 ablation setup. The interference between the beam reflected from the fiber end facet and the surface of the object slide is observed with the microscope. The interferogram of a fiber mirror profile in (b) has radii of curvature in horizontal and vertical direction: $R_h = (152 \pm 8) \mu\text{m}$ and $R_v = (145 \pm 7) \mu\text{m}$.

from the front side of the object slide is not disturbing the interferogram, because the plate has a thickness of 1 mm and therefore much larger than the coherence length. The object slide can be removed with a nanometer translation stage during the ablation.

3.5.3 Mirror parameters

The mirror profiles can be determined from the interferograms of both profilometer in the same way. In both cases the height difference in the mirror profile between two maxima is $\lambda/2$. The distance between the extrema is calibrated by the known diameter of the fiber. As shown in Fig. 3.12(a) the profile is approximately Gaussian shaped. The central region serves as the mirror. The diameter of the structure has to be chosen large enough with respect to the cavity mode diameter to reduce clipping losses. The most important parameter of the profile is the radius of curvature R in the central region of the profile. In the example of Fig. 3.12 the local radius of curvature is determined in (b) and for the interval of $[5, -5] \mu\text{m}$ the central region can be approximated with a circular segment as shown in (c) [11]. Therefore, the radius of curvature is determined from the interferogram as the following:

The path length difference $2z_r = r^2/R$ (with r the distance from the center) between the beam from the plane reference surface and the beam with a Gaussian shaped profile is given by Eq. (2.7). The interference pattern of the beams with amplitudes I_A and I_B is then given by:

$$I(r) = E^2(r) = I_A^2 + I_B^2 + 2I_A I_B \cos\left(\frac{2\pi}{\lambda} \frac{r^2}{R}\right) \quad (3.5)$$

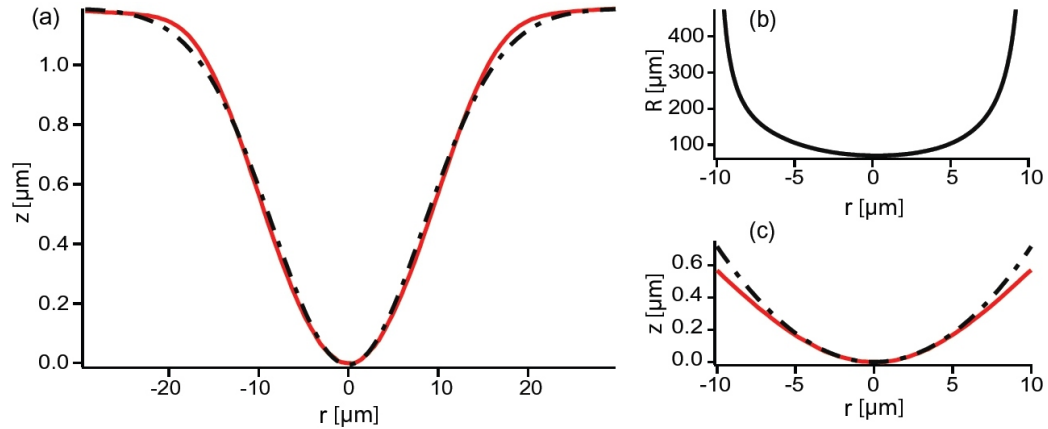


Figure 3.12: (a) the red solid line is a cut through the profile based on the data of a profilometer. The shape is nearly Gaussian shaped as the dashed line shows. (b) is the local radius of curvature obtained from a tenth-order polynomial fit to the data in (a). In (c) is a detailed view from the central region from (a) and a section of a circle with a radius $R = 70 \mu\text{m}$ [11].

and the condition for an extremum in the interference pattern is then given by

$$r_0^2(p) = p \frac{R\lambda}{2}, \quad p = 1, 2, \dots \quad (3.6)$$

From the interferogram we can extract the information of the distance $r_0(p)$ of the 'p'th maximum and with the known wavelength the radius of curvature R can be fitted. Typically the radius is fitted from p extrema for a fit radius $r_0(p) < (5 - 10) \mu\text{m}$ in vertical and horizontal direction of the interferograms of both profilometer. The achieved radii of curvature with the ablation setup in Paris are shown in Fig. 3.13.

Discussion

The quality of both interferogram is very good for an optical evaluation. The radius of curvature is determined with a software, which makes a fit of Eq. (3.6) to the interferogram of a profilometer image. The uncertainty for the radius of curvature is estimated with this software to be 10%. The contrast of the interference pattern with the Fizeau interferometer is better since the maximal intensity of both interfering beams I_A and I_B is almost equal. The difference is larger for the Mirau profilometer because the mirror inside the Mirau objective backreflects more light than the fiber surface.

A further difference between both profilometer types is the working distance d_{work} . For the Mirau profilometer d_{work} is 4.7 mm and for the Fizeau profilometer $65 \mu\text{m}$ limited by half the coherence length. Since the maximum contrast of the interference pattern is achieved, when the object slide almost touches the fiber end facet, the object slide has to be positioned carefully in order to avoid this contact between the two surfaces. Furthermore the Fizeau profilometer has an financial advantage since the Mirau objective is much more expensive than the other optical parts. But beyond that, the Fizeau profilometer can be implemented into the ablation setup. This improves the alignment of the microscope, which is used for a visual alignment

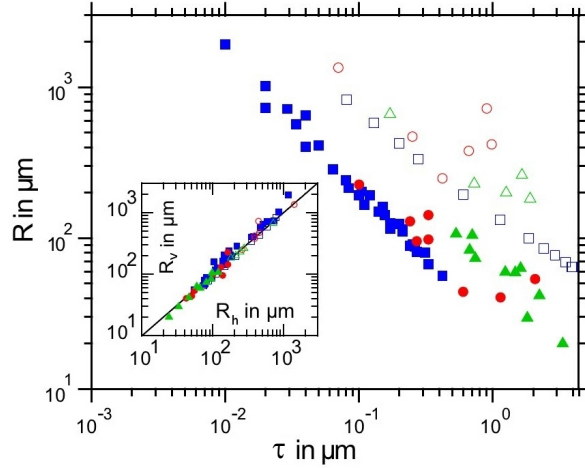


Figure 3.13: Radius of curvature R of fabricated mirror profiles with the ablation setup in Paris determined with a profilometer dependent from the laser power, the beam waist and the illumination time: ■ 600 mW, 26 μm ; □ 1.85 W, 73 μm ; ● 373 mW, 27 μm ; ○ 900 mW, 63 μm ; ▲ 540 mW, 28 μm ; △ 575 mW, 63 μm . In the inset the ratio between the vertical and horizontal radius of curvature is shown and indicates a circular shape of the fabricated mirrors [18].

of the fiber end facet. The reason is, that the center of the structure is determined from the contours of the profile in the microscope image within a few micrometers and with the included interferogram the precision increases to about 1 μm .

The profile of structures with a small depth can be determined more precisely with a light source with a lower wavelength since more extrema are observed within the same fit radius. The large difference of the coherence length between 9 μm and 130 μm of the profilometer becomes visible for deep structures. With the Mirau profilometer the interference pattern is not visible for the whole structure in one picture and the Gaussian fit gets less precise. But there is an opportunity to take advantage of the short coherence length of the Mirau profilometer. Here the probe is moved along the beam direction z . For each pixel the intensity distribution is formed by a Gaussian envelope and a periodic modulation with a period of $\lambda/2$ as shown in Fig. 3.14(b). The defined z position for the maximum intensity is determined for all pixels. The topography of a fiber mirror with this method is shown in Fig. 3.14(a).

3.6 Minimization of the astigmatism

In Fig. 3.5 astigmatism of the CO₂ laser beam is observed. We found out, that the dichroic mirror is mainly responsible for the astigmatism. This aberration occurs since this plane plate is placed with a tilt of 45° in the focused Gaussian CO₂ laser beam. The effect of the dichroic mirror is shown in the following measurement in Fig. 3.15. Structures are fabricated on a fused silica plate around the focal point once with the dichroic mirror and once without the dichroic mirror. The important parameters, the radii of curvature R_v , R_h are determined with the Mirau profilometer in vertical and horizontal direction since they corresponds to the major and minor axis of the elliptical structure. The latter is reasonable since the symmetry axis of the tilted dichroic mirror are in the vertical and horizontal plane. The ratio R_v/R_h is a quan-

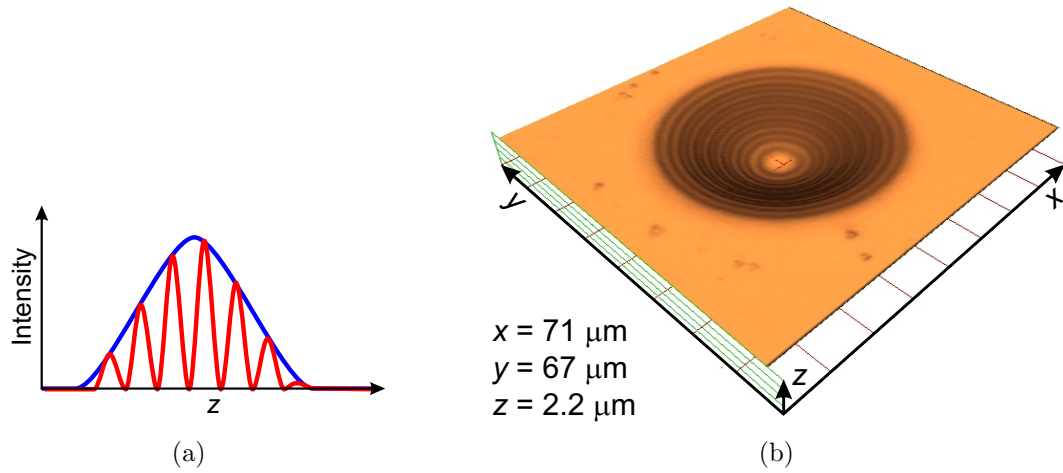


Figure 3.14: Advanced Mirau profilometer: Here the probe is moved along the beam direction z . For each pixel the intensity distribution in sketch (a) is formed by a Gaussian envelope and a periodic modulation with a period of $\lambda/2$. The z position for the maximum intensity is determined for all pixels. A measured topography of a fiber mirror with this method is shown in (b).

titative parameter which describes the ellipticity. The uncertainty of the position is estimated with $2 \mu\text{m}$ and for the radii of curvature with 10% of the value.

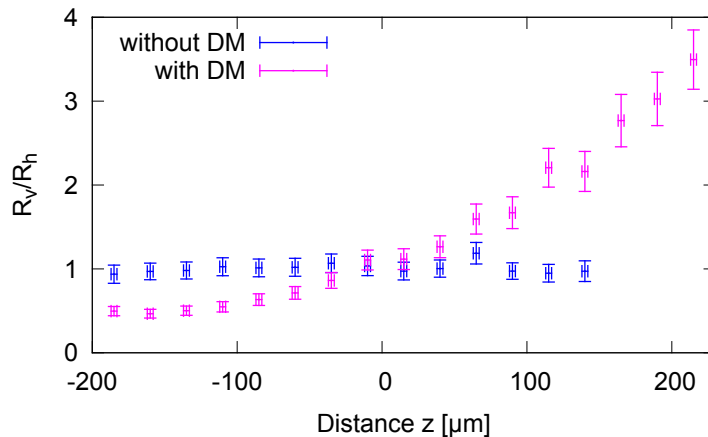


Figure 3.15: The tilted dichroic mirror in the focused beam causes primarily the observed astigmatism. The ratio between the radius of curvature in vertical and horizontal direction of structures on a silica plate are determined at different position around the focal point. In blue the ablation process is done without ($P = 1.4 \text{ W}$, $w_0 = 32 \mu\text{m}$) and in magenta with the dichroic mirror ($P = 2.0 \text{ W}$, $w_0 = 32 \mu\text{m}$).

Discussion

With the dichroic mirror a large ellipticity is observed as expected. Without the dichroic mirror the ratio stays constant at 1 ± 0.06 . It was also observed, that a tilted lens in the ablation setup also leads to astigmatism. But this effect is within the measurement uncertainty and therefore negligible. Furthermore the CO_2 laser beam has an initial ellipticity of about $M^2 = 1.1$ which can also explain the deviation of 6% in the measurement without the dichroic mirror.

With this knowledge of the astigmatism, the ablation parameter w_r can be changed in a simple way. The mirror is just removed along the beam direction and the different beam radii around the focal point can be used to fabricate different structure.

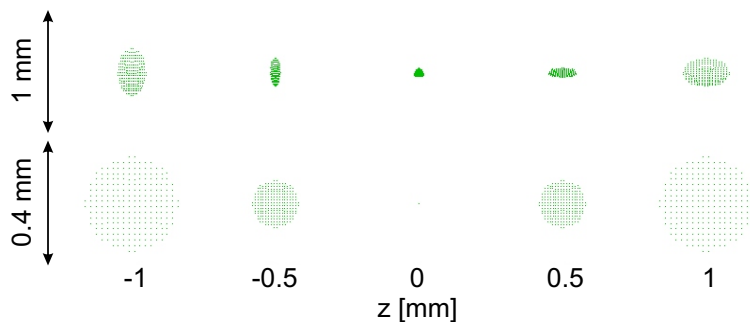


Figure 3.16: Simulating the beam profile behind the third lens around the focal point. The deformed profiles in the upper row are received with a tilted plate with a thickness of 2.5 mm and a refractive index of $n = 2.4$. Without the dichroic mirror the profiles are circular as expected as it is seen in the lower row.

The measurement was also simulated with the simulation program OSLO¹³ by Gaussian ray tracing. In Fig. 3.16 one can see in the first row the situation with the dichroic mirror and in the second row the case without the dichroic mirror. An ideal Gaussian CO₂ laser beam was assumed and a plate with a thickness of 2.5 mm and a refractive index of ZnSe $n = 2.4$. Aberrations are observed for the case with the dichroic mirror and a circular shaped beam without the plate. Furthermore one can see, that the beam waist is larger with the dichroic mirror. The measurement in Sec. 3.4 has to be repeated if the ablation process is done without the dichroic mirror since the waist size and the waist position are then different. Furthermore the dichroic mirror has to be placed reproducibly into the setup within nanometer precision since the microscope is used for the visual alignment. Possible solutions might be a tiltable mirror, a mirror placed on a translation stage or kinematic base. A further solution is the use of a dichroic mirror reflective for the CO₂ laser and transparent for visible light.

3.7 Reproducibility

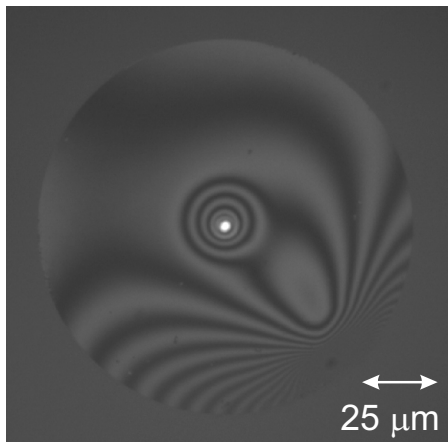


Figure 3.17: By the determination of the center of the structure (interferogram) and the fiber core (white spot) and by comparing the two for different fiber mirrors, the stability of the CO₂ laser beam position is investigated. Parameters of the shoot are $w_0 = 38 \mu\text{m}$, PWM frequency = 10.5 kHz, pulse length $\tau = 8 \text{ms}$. One can also see the cleave artefacts at the edge of the fiber surface.

For reproducible results of the fabricated mirrors two things are important. On one hand a stable fiber mounting and on the other hand a stable CO₂ laser beam. There was the suspicion, that the position of the laser beam is not stable in time. This is determined with the following measurement.

¹³SINCLAIR OPTICS

dx_h [μm]	-0.20	-0.21	0.02	-0.82	0.92	0.4	-0.12
dx_v [μm]	-0.70	-0.02	0.36	0.85	-0.57	-0.31	0.38
dr [μm]	0.73	0.21	0.36	1.18	1.08	0.51	0.40
σ [μm]	0.37						

Table 3.1: Stability of the CO₂ laser beam: Measurement of the variation of the center of the structure with respect to the fiber core with dx_h and dx_v the variation in horizontal and vertical direction respectively, dr their resolving radius and σ the standard deviation from dr .

Seven fiber mirrors are fabricated under the same conditions. Each time the center of the fiber core is aligned to the center of the CO₂ laser beam with the microscope. In the next step the two centers are determined. Therefore, the core is illuminated with a fiber checker which is adjusted at the other end of the fiber as shown in Fig. 3.17. The core appears as a white spot with a diameter of about 5 μm and the center can be measured. The center of the structure is determined with the Mirau profilometer. In the same figure the interferogram is shown. The two centers can be extracted from the same picture since the fiber core appears at the same position before and after the ablation process. Also a slight change in position or angle, which appears between different fiber analyses, has no significant effect on the position of both centers. Since the Fizeau profilometer was not yet implemented at that time, a picture of the fiber end facet is taken in the ablation setup and in the profilometer setup. A systematical constant error like that from a misalignment of the microscope can be compensated afterwards. The orientation of the fiber end facet is reconstructed thanks to the cleave artefacts on the fiber surface. By comparing the position of the two centers the stability of the CO₂ laser is estimated. The following uncertainties are taken into account: An uncertainty of 1 μm has to be considered due to the optical alignment of the fiber. For the determination an uncertainty due to the camera resolution of about 200 nm has to be taken into account, as well as the uncertainty of 500 nm for the determination of the centers. This leads to a total uncertainty of 1.1 μm

Discussion

The position of the structure center was determined with respect to the core center. The measurement points are distributed around a point at a distance of 1.5 μm from the core which is on the order of the uncertainty of the alignment of the microscope. As a consequence the CO₂ laser is not centered to the center of the core during the ablation process. This constant offset of $\delta x_h = (1.2 \pm 0.5) \mu\text{m}$ and $\delta x_v = (-0.9 \pm 0.5) \mu\text{m}$ is deducted from the values and the final result is shown in Tab. 3.1. The uncertainty of the laser position varies about 400 nm with a maximal measured deviation of 1.2 μm . Therefore, the stability of the CO₂ laser is stable within the measurement accuracy.

3.8 Coating

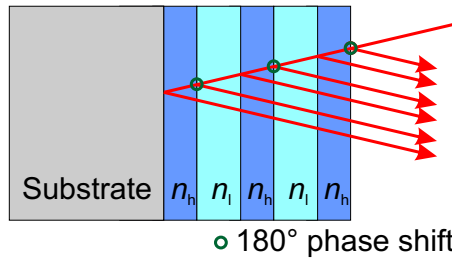


Figure 3.18: Principle of a dielectric mirror: Constructive interference due to a multilayer of alternate high and low refractive index films.

The reflectivity of the fiber mirror with 4% can be increased to a reflectivity larger than 99.99% with a dielectric coating. The principle of a dielectric coating is shown in Fig. 3.18. The coating consists of a multilayer of alternate high and low refractive index films n_h and n_l , which have a thickness $t_{h/l} = \lambda/(4n_{h/l})$. A part of the incident beam is reflected at each interface. Including the phase shift of 180° of the reflected beam at the interface of material n_h , all reflected beams interfere constructively. The reflectivity $R_{\mathcal{F}}^*$ of two layers is then given by

$$R_{\mathcal{F}}^* = \left(\frac{n_h - n_l}{n_h + n_l} \right)^2. \quad (3.7)$$

A very successful technique to coat the fibers is the ion beam sputtering (IBS) because the surface roughness and the intrinsic stress are lower compared to other coating techniques. The fiber preparation and the coating run take place as follows. Since residues like dust on the fiber mirror reduce the surface roughness significantly, the mirrors have to be cleaned just before the coating process outside the vacuum chamber of the coating machine. Consecutively each fiber is cleaned in an aqueous solution of HCl, an ultrasonic bath, H₂O and finally in acetone each time for 2 min [11].

Ion beam sputtering

In a vacuum chamber a high energy ion beam (argon) strikes the obliqued solid target sketched in Fig. 3.19. To deposit layers of different material during the coating process, several solid targets are mounted on a turret. Dislodged molecules from the solid target with a main impulse in the direction of the substrate, coat the surfaces inside the chamber. The fiber is mounted on a rotatable and translational shaft to increase the homogeneity of the layers. The thickness of a layer is supervised with a crystal quartz monitor. It is placed next to the substrate and coated with the same layer as the fiber end facet. Connected to an oscillator circuit, it changes the frequency depending on the mass deposition.

With this technique¹⁴ a low surface roughness around 1 Å and low intrinsic stress of about a few 100 MPa is reached.

¹⁴ATFilms, Boulder

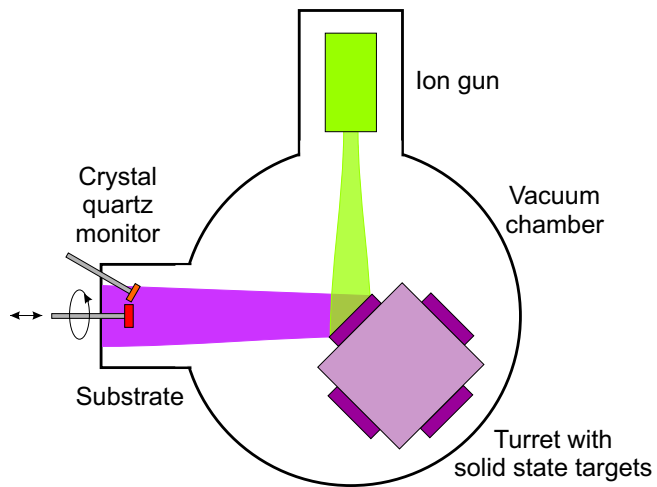


Figure 3.19: Ion beam sputtering: An argon ion beams strikes a solid target mounted on a turrent, where molecules are dislodged. They deposit on the surface of the substrate that has to be coated. The layer thickness is supervised with the crystal quarz monitor.

4 Fabrication of fiber mirrors in Bonn

The ablation setup in Bonn is an improved version of the one in Paris. The dichroic mirror is substituted by a removable silver mirror to reduce astigmatism. Furthermore, the mirror is used to implement a Michelson interferometer as a new approach to measure the mirror profiles and a new method to align the fiber end facet in the setup is introduced. First structures are fabricated and one profile is measured with an atom force microscope with a precision of about 10 nm.

4.1 Ablation setup

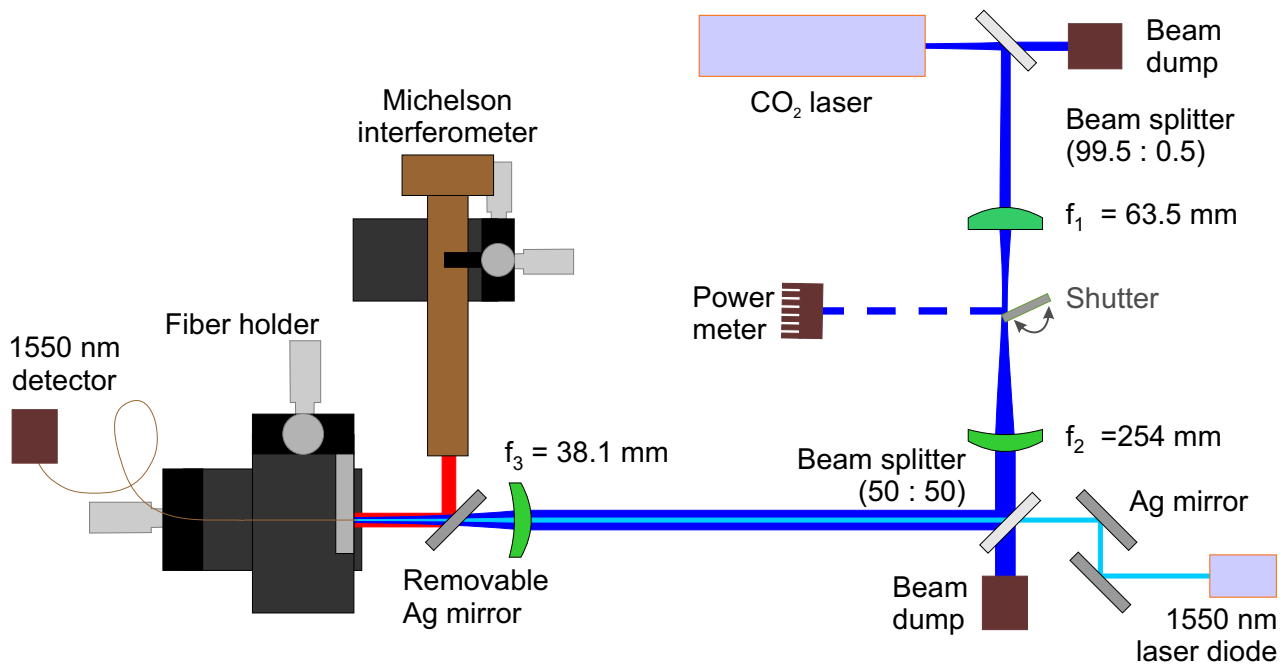


Figure 4.1: CO₂ ablation setup in Bonn.

The new ablation setup is shown in Fig. 4.1. The CO₂ laser¹⁵ has a maximum output power of 30 W. The beam has a waist diameter of (2.5 ± 0.5) mm with a divergence angle smaller than 7 mrad. Furthermore the mode quality is $M^2 < 1.2$. The beam is expanded by the Keplerian telescope with a magnification of 4. The collimated beam is focused with a third lens onto the fiber end facet. By assuming an ideal gaussian beam the waist is estimated in the focal point with $13 \mu\text{m}$. Due to the damage threshold of the power meter¹⁶, the sensor head of the device is placed behind the first beamsplitter (99.5:0.5) for a laser beam power larger than 6 W. For a small beam power, the sensor head is positioned in the beam deflected by 90° by the closed shutter. The shutter is made of a copper mirror moved by a servo motor and has a transit time for a deflection angle of 80° of about 40 ms. The fiber is aligned by three

¹⁵FIRESTAR v30 (water cooled), SYNRAD

¹⁶PM100D, THORLABS GmbH, sensor head: S310C

perpendicular stages¹⁷ controlled by a stepper motor which includes a high position feedback which enables a positioning within a precision of 100 nm. The fiber end facet is observed with a Michelson profilometer which is explained in chapter 4.3. For the observation a silver mirror is placed under 45° into the beam path in front of the sample. For the characterisation of the surface structure, the position of the silver mirror has to be reproducible within a few micrometers.

The fiber end facet is initially aligned with the microscope as in Paris. This will be improved with the help of a 1550 nm laser diode which is overlapped with the CO₂ laser beam using a 50:50 beam splitter. 1550 nm light is transmitted through the fiber and detected by a photodiode. In this way, the position of the fiber end facet can be determined by the amount of light coupled into the fiber.

The two lasers, the shutter and the stages are controlled by a single microcontroller¹⁸ which is operated by a computer. The circuit diagram for the MBED and the devices in the ablation setup is shown in App. A. The timing sequence for the ablation process is the same as the one in Paris shown in Fig. 3.4.

4.2 Power stability and ablation parameters

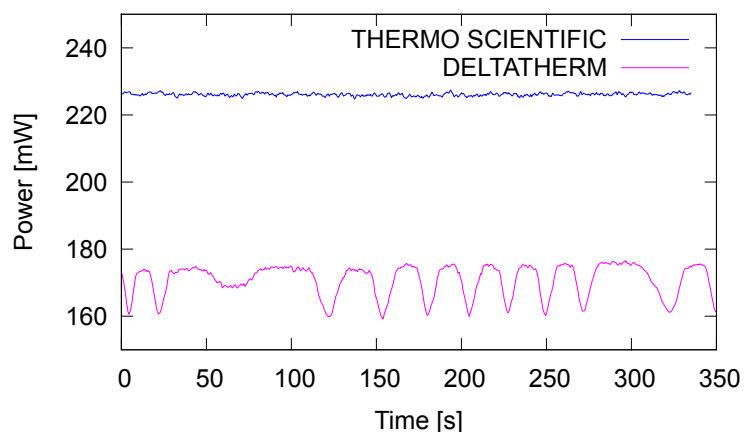


Figure 4.2: The CO₂ laser beam power is measured during the use of the chiller from THERMO SCIENTIFIC with power fluctuations of $\pm 0.4\%$ after the heat up phase and during the use of the chiller from DELTATHERM with power fluctuations of $\pm 5\%$. This measurement shows, that the power fluctuations of the laser are smaller than $\pm 0.4\%$ and larger fluctuation are caused by the DELTATHERM chiller.

After the heat up phase of 20 minutes the power fluctuations reduces to $\pm 5\%$ as shown in

¹⁷MFA-CC, NEWPORT

¹⁸NXP LPC1768, MBED

Fig. 4.2, which is within the specification of the chiller¹⁹ for the CO₂ laser. The CO₂ laser power is also measured for a different chiller²⁰ and the fluctuations reduces to 0.4%. Therefore, the power fluctuation of the laser are smaller than 0.4% and the higher fluctuations are induced by the DELTATHERM chiller. Since the periodicity of the fluctuations by the DELTATHERM chiller is in the order of 30s, and therefore much longer than the time of the ablation process in the order of 100 μ s, the ablation process is triggered when a threshold power is exceeded. The maximal variation in power within a period of the illumination time is then estimated to 0.1% which enable reproducible processes.

As expected the beam profiles around the focal point shown in Fig. 4.3 are circularly shaped without significant aberrations. Therefore, the beam radius can be changed by moving the fiber along the beam direction. The duty cycle which controls the power of the CO₂ laser, the position along the beam to adjust different beam radii and the illumination time are changed via the microcontroller.

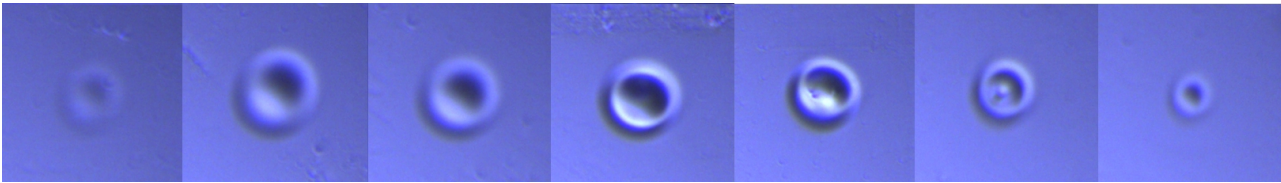


Figure 4.3: Fabricated structures on an object slide in 250 μ m steps around the focal point which is at a position between the fourth and fifth image: As expected the beam profiles does not show large aberrations along the beam direction. The beam radius can be changed by moving the fiber along the beam direction.

4.3 Michelson profilometer

The profilometer used in Bonn is sketched in Fig. 4.4(a). The light from a 505 nm LED is split in two beams. In each arm the beam passes an identically constructed objective²¹ (10x magnification) and is then focused onto the fiber end facet or onto a plane reference surface of an object slide. The backreflected light is recombined and observed with a CCD camera. The objective slide is mounted on a $XY\theta\varphi$ stage.

Discussion

As the Fizeau profilometer, this profilometer has the advantage, that it can be implemented into the ablation setup, it has low costs and a good contrast in the interferogram, since the two surfaces reflect almost the same amount of light back. But it also has the advantage like the Mirau profilometer of a long working distance, in this case of about 23 mm. A first interferogram is observed as shown in Fig. 4.4(b), but the alignment is very difficult since the two

¹⁹LT MINI 0.8, DELTATHERM

²⁰NESLAB MERLIN M25, THERMO SCIENTIFIC

²¹SPINDLER & HOYER

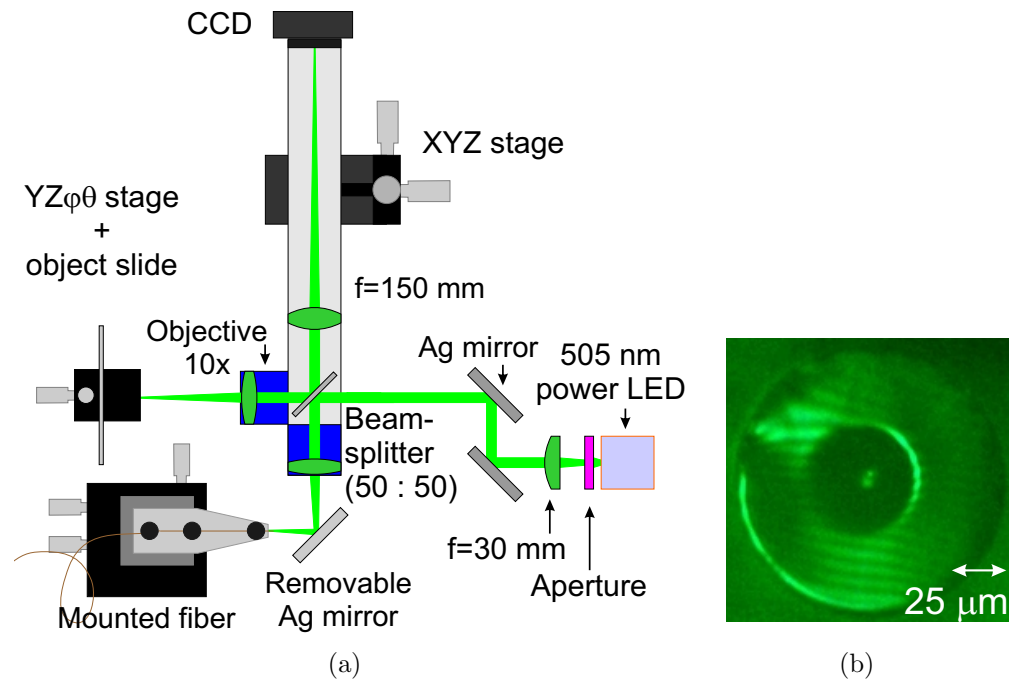


Figure 4.4: Michelson profilometer: (a) The profilometer is implemented into the ablation setup. To observe the fiber end facet a removable silver mirror is placed in front of the fiber at an angle of 45° . The interference of the backreflected light from a fiber end facet and the reference surface of an object slide in (b) is observed with a CCD camera.

beam paths of about 5 cm have to be matched within half the coherence length of about $5 \mu\text{m}$. To increase the coherence length, a band pass filter of 3–10 nm will be implemented.

4.4 First characterisation

A method to determine the profile with nanometer precision is the use of an atomic force microscope (AFM) sketched in Fig. 4.5(a). Here the attraction caused by Van der Waals forces between the sample surface and a thin tip on a cantilever is measured. With a feedback circuit the flexible cantilever stays in constant distance to the surface which corresponds to a certain amount of measured attraction. The sample is scanned and a laser beam is continuously measuring the vertical position of the tip. To investigate a whole profile, a small structure is fabricated on a fiber end facet, since the AFM has a limited scan region of $50 \times 50 \mu\text{m}$ and the result is shown in Fig. 4.5(b).

Discussion

A Gaussian profile fits to the vertical and horizontal cut of the profile as shown in Fig. 4.6. For two perpendicular cuts the $1/e^2$ diameter of $2\sigma_1 = 6.6 \mu\text{m}$ and $2\sigma_2 = 7 \mu\text{m}$ are measured. Since no significant aberrations are observed, the cuts are chosen randomly. With a deviation of 5% circular Gaussian shaped structures are produced with the ablation setup.

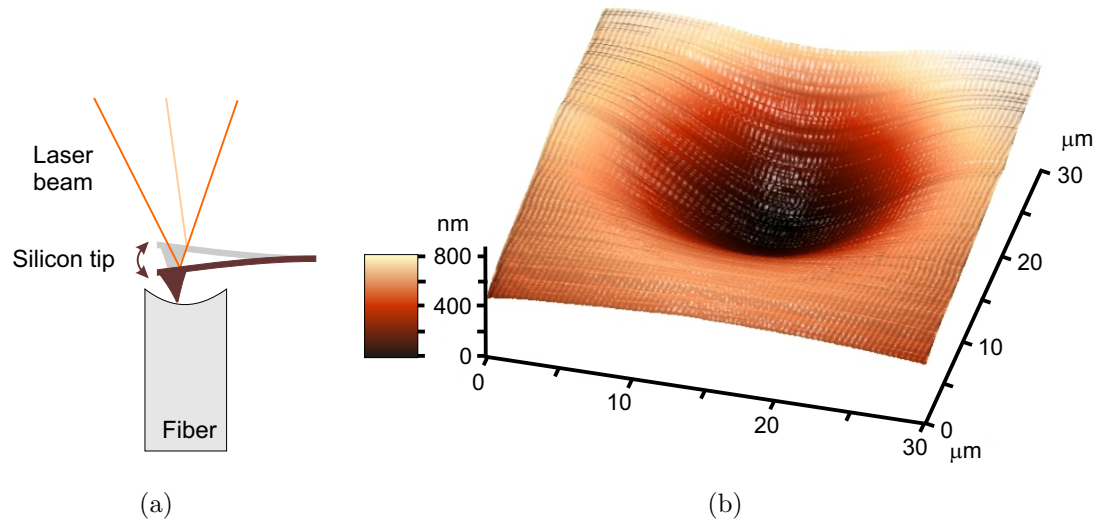


Figure 4.5: Atomic force microscope: (a) A thin silicon tip on a cantilever is attracted to the sample surface depending on the distance between the two due to the Van der Waals forces. The position of the tip is measured with a reflected laser beam. (b) shows the result of a circular shaped mirror profile on a fiber end facet (PWM 5 kHz, $P=700$ mW).

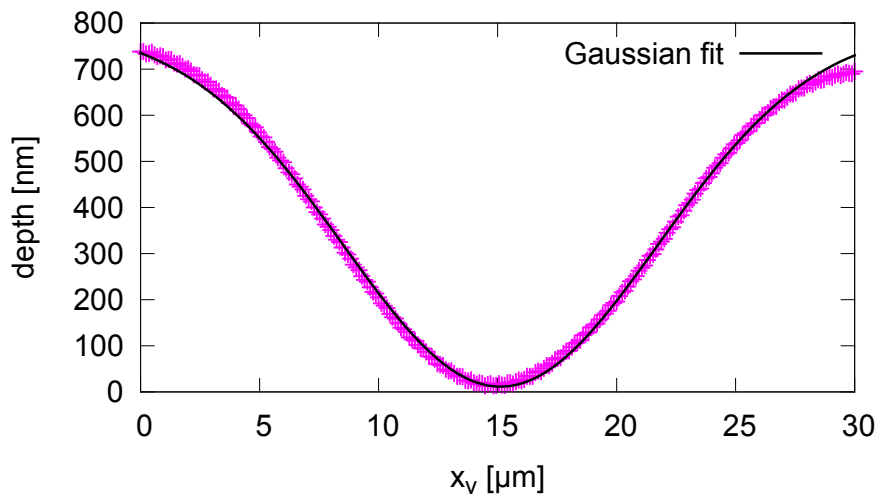


Figure 4.6: Cut through a mirror profile on a fiber and facet measured with an AFM: The profile of the cut (magenta) is almost Gaussian shaped as the black solid fit line shows.

4.5 Fiber holder

The mirror coatings from ATFilms in Boulder are presently the best coatings with the desired reflectivity and surface roughness. Since the company has a special mounting for the fibers in the vacuum chamber, we designed a new fiber holder, which can carry 390 fibers. This holder is shown in Fig. 4.7 and consists of 16 single metal plates, each one having 26 V-Grooves. Therefore, the plates form 15 layers in which the fibers with a protective PTFE tubing are clamped by screwing the plates together. Finally a metal protection for each layer of fibers, which also include a V-groove, is placed onto the proceed fiber and the holder can be safely

transported.

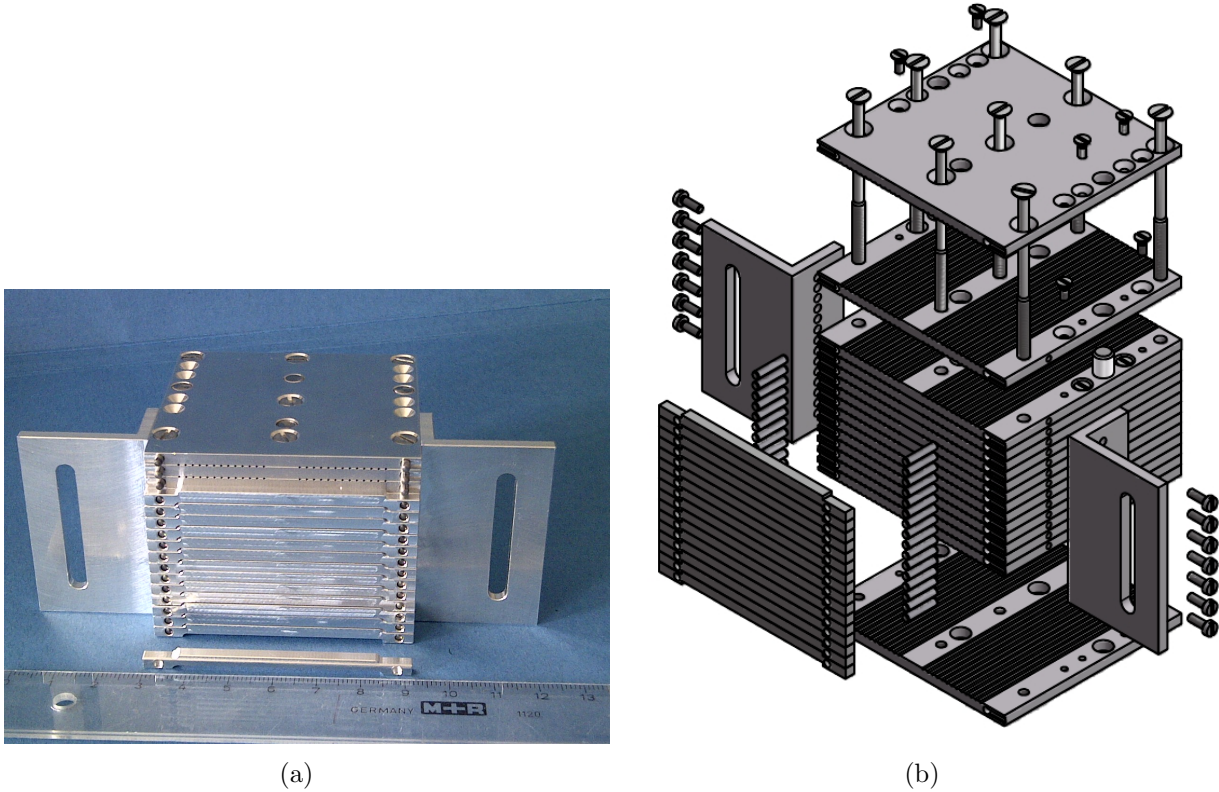


Figure 4.7: Fiber holder.

5 Characterisation of a fiber cavity

The topic of this chapter is the assembly, alignment and characterisation of a fiber Fabry-Pérot cavity in Paris. The important parameters are the properties of the cavity like the free spectral range or the finesse and the properties of the mode field in the cavity like the mode waist and the cavity field decay rate. Furthermore the birefringence of the mirror coatings was investigated which is observed as a resonance splitting in the transmission signal.

5.1 Fiber Fabry-Pérot cavity

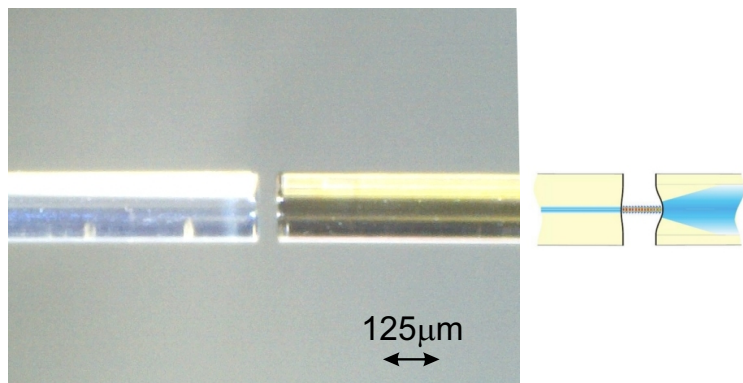


Figure 5.1: The fiber Fabry-Pérot cavity consists of a singlemode fiber (left) and a multimode fiber (right). The multimode fiber appears darker due to an additional carbon cladding. The mirrors have radii of curvature of $50\ \mu\text{m}$ and $500\ \mu\text{m}$. Laser light at a wavelength of $\lambda = 896\ \text{nm}$ is coupled in through the singlemode fiber.

For a fiber cavity in high vacuum with a pressure of 10^{-10} – 10^{-11} mbar copper coated fibers are used since the degassing is lower as well as the diffusivity of hydrogen and the mounting is more stable compared to a fiber with an acrylate jacket. The fiber Fabry-Pérot cavity shown in Fig. 5.1 consists of a singlemode fiber²² and a multimode fiber²³ with a diameter of $125\ \mu\text{m}$. The multimode fiber appears darker due to an additional carbon coating. The radii of curvature of the two mirrors are $50\ \mu\text{m}$ and $500\ \mu\text{m}$. Each mirror is coated with 64 alternating layers of SiO_2 ($n=1.479$) and Ta_2O_5 ($n=2.078$) for $\lambda = 900\ \text{nm}$ by ATFilms in Boulder (USA).

5.2 Characterisation setup

The characterisation setup is shown in Fig. 5.2. Behind a diode laser with an optical power output of about 10 mW and a measured wavelength of $\lambda = 896\ \text{nm}$, a prism pair transforms the elliptical shaped beam into a nearly circular shaped beam and an isolator reduces laser light reflection back into the laser. The polarisation of the laser is adjusted for the PM fiber coupled electro-optic modulator²⁴ (EOM) by using a $\lambda/2$ -plate. Two sidebands with a frequency difference of $\pm 2\ \text{GHz}$ are added by the EOM for a frequency calibration of the cavity transmission signal. The EOM is driven with an RF generator²⁵ with an amplified²⁶ output power up to 630 mW. It is possible, to couple a second wavelength at 830 nm into the cavity with the help

²²SM800-125CB

²³G150-125CB

²⁴NIR-MPX800-LN-10, PHOTLINE TECHNOLOGIES

²⁵E8257D, AGLIENT TECHNOLOGIES

²⁶ZVA-213+, MINI-CIRCUITS

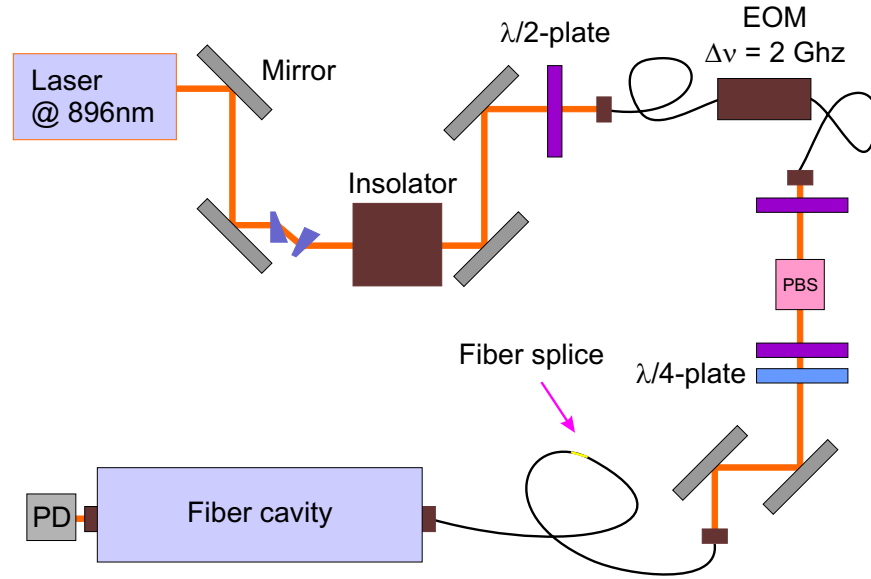


Figure 5.2: Scheme of the characterisation setup to determine the properties of a fiber cavity.

of a polarising beam splitter. With a $\lambda/2$ - and $\lambda/4$ -plate for $\lambda = 850$ nm the light, which is coupled into the cavity, becomes elliptically polarised. The transmission signal is measured with a photodiode²⁷ at the other end of the multimode fiber and the signal is visualized with an oscilloscope. Since the input resistance of the oscilloscope of $1\text{ M}\Omega$ is reduced by a parallel-connected resistance to $R_{\text{Osz1}} = 1\text{ k}\Omega$, the bandwidth f_{BW} of the photodiode with a capacity of $C = 40\text{ pF}$ is increased to

$$f_{\text{BW}} = \frac{0.35}{CR_{\text{Osz1}}} = 8.8\text{ MHz} \quad (5.1)$$

5.3 Alignment

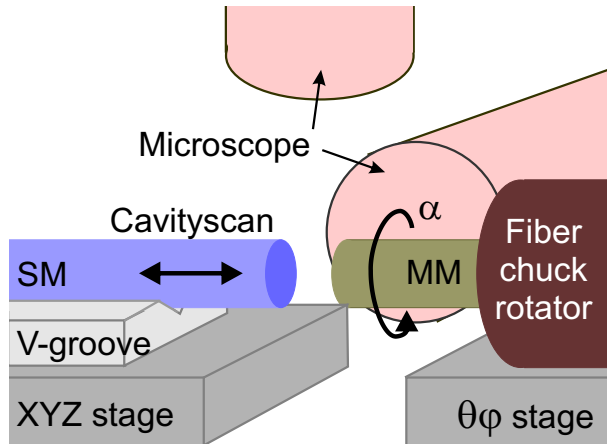


Figure 5.3: Cavity alignment: The singlemode fiber is mounted in a V-groove on an XYZ positioning stage and the multimode fiber in a fiber chuck rotator on a $\theta\phi$ positioning stage. The cavity is observed with two perpendicular adjusted USB microscopes. The cavity length is varied by a length corresponding to λ by actuating shear piezos attached to the singlemode fiber. The multimode fiber is rotated to investigate birefringent effects.

²⁷DET36A, THORLABS

The singlemode fiber is mounted in a V-groove on a XYZ nanometer precision stage²⁸ as shown in Fig. 5.3. The MM fiber is positioned in a fiber chuck rotator²⁹ on a $\theta\varphi$ positioning stage and can be rotated 360° around the cavity axis to investigate birefringent effects. Two 400x USB microscopes³⁰ are placed perpendicular to each other around the cavity. The cavity length is varied by a length corresponding to λ by actuating shear piezos attached to the singlemode fiber.

The coupling of the light into the singlemode fiber just by observing the cavity transmission signal is difficult, since there are five degrees of freedom to couple the light into the singlemode fiber and five degrees of freedom for the cavity alignment to observe a transmission. Therefore, the following simplifying method is used. The light is coupled into a singlemode fiber which corresponds to the singlemode fiber with the cavity mirror, but with two cleaved end facets. The coupling is optimized and then the two fibers are spliced together. In this way the incoupling of the light into the cavity is maximized and in a further step the fundamental mode is aligned as well as the outcoupling of the light via the transmission signal.

The cavity is aligned as follows. First a rough adjustment is done with the help of the two camera images. To measure then a transmission signal, both mirrors are brought very close to each other without contact. With the stages the transmission is increased further and the cavity length is increased to the desired length. The angle θ is scanned to verify, that only the fundamental cavity mode is supported. At an angle of more than 10° resonance peaks of higher transversal modes arise. Furthermore the current of the laser is scanned to verify the singlemode operation of the laser as far away as possible from a mode jump. Since the voltage amplitude of the piezo is set for a scan over two free spectral ranges, the observation of two final modes in the transmission signal verifies, that the fundamental mode is aligned.

5.4 Characterisation

For the characterisation the multimode fiber is rotated stepwise by 23° and after each step the cavity is realigned to the same cavity length. Then the camera images and the transmission signal from the photodetector are stored. Since the cavity is not protected by any shielding, large fluctuation in the transmission signal are observed due to disturbances like air flow and vibrations. Therefore, the averaged value from five images is determined in each measurement. From the camera picture the cavity length L as shown exemplarily in Fig. 5.1 is determined and calibrated to the known fiber diameter. The free spectral range, the half width half maximum of the resonance peak and the resonance splitting are measured from the transmission signal. The quantities are calibrated by the two sidebands added by the EOM with an adjusted difference of 4 GHz as shown in Fig. 5.4 with

$$1 \mu\text{s} \hat{=} (108.6 \pm 6.6) \text{ MHz} \quad (5.2)$$

²⁸3-Axis NanoMax, THORLABS

²⁹HFR001, THORLABS

³⁰VMS-004D, VEHO

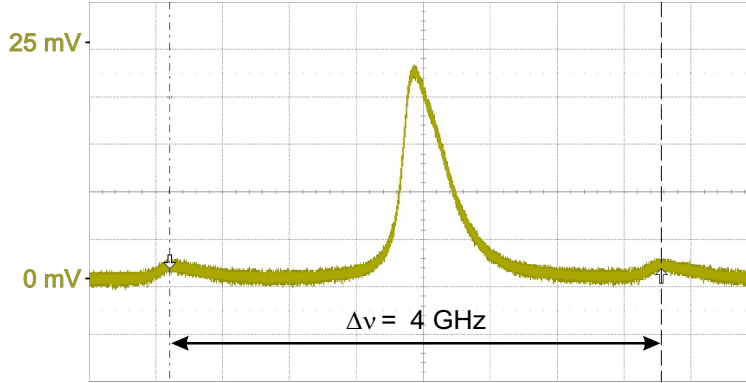


Figure 5.4: Calibration of the transmission signal. The parameter of the transmission signal, namely the half width half maximum, the free spectral range and the resonance splitting are calibrated to the frequency domain by the sidebands of the incoupled beam. The difference of the sidebands $\Delta\nu = 4$ GHz around one resonance peak corresponds to twice the RF frequency of the EOM. The significant asymmetry is mainly coming from two resonances close to each other with different amplitudes.

5.4.1 Cavity length, free spectral range and finesse

Since the free spectral range depends only on the cavity length L as shown in Eq. (2.18) by assuming a refractive index $n = 1$, the two parameters are independently determined from the camera images and the transmission signal. The measured value of the cavity length is $L = (23 \pm 2) \mu\text{m}$ and the calculated free spectral range is given by $\Delta\nu_{\text{FSR}} = (4.3 \pm 0.4) \text{ THz}$. From the transmission signal a free spectral range of $\Delta\nu_{\text{FSR}} = (6.6 \pm 0.7) \text{ THz}$ is measured and the cavity length $L = (35 \pm 3) \mu\text{m}$ is calculated. With a full resonance width at half maximum $\delta\nu = 450 \pm 103$ and the averaged value of the determined free spectral ranges the finesse is given with Eq. 2.19 by $\mathcal{F} = 7667 \pm 2138$.

Here the following uncertainties are considered: Since the cavity is scanned by changing the length L , an uncertainty $\Delta L_1 = 1 \mu\text{m}$ has to be considered. An uncertainty for the measured cavity length is given by the camera resolution of $1.5 \mu\text{m}/\text{pixel}$ and the standard deviation from all measurement points $\Delta L_2 = 3.8 \mu\text{m}$. Since the fibers are externally illuminated, bright reflections appear on the fiber surface and the fiber diameter seems to be larger and the cavity length L smaller than it is in reality. The error is therefore estimated to be $\Delta L_3 = 3 \mu\text{m}$. The uncertainty for the measured free spectral range and the finesse is estimated by the standard deviation of the width of the resonance, the free spectral range and the calibration of all measurements.

Discussion

Between the results of the measurement by the camera images and the measurement from the transmission signal is a significant deviation which can not be explained by the assumed uncertainties. One reason can be the unprecise imaging by the USB microscopes since it is unknown if the scaling of the pictures in vertical and horizontal direction is equal which would lead to a wrong calibration of the cavity length. Another reason might be a nonlinear piezo scan since the piezo is controlled without any feedback (open loop operation) which might have a significant effect on calibrating the FSR in milliseconds with the sideband difference in the microsecond range. This could not be investigated further during this work because my stay in the group of Prof. Reichel in Paris where this setup is located was over and I came back to Bonn. As a

Parameter	Symbol	value
Cavity length ^a	L [μm]	23 ± 2
Cavity length ^b	L [μm]	35 ± 3
Cavity length ^c	L [μm]	27 ± 8
Free spectral range ^a	$\Delta\nu_{\text{FSR}}$ [THz]	4.3 ± 0.4
Free spectral range ^b	$\Delta\nu_{\text{FSR}}$ [THz]	6.6 ± 0.7
Free spectral range ^c	$\Delta\nu_{\text{FSR}}$ [THz]	5.5 ± 1.6
Resonance width ^b [MHz]	$\delta\nu$	450 ± 103
Finesse ^{b,c}	\mathcal{F}	7667 ± 2138
Reflectivity ^{b,c} [%]	$R_{\mathcal{F}}$	99.96 ± 0.01
Mode waist [μm]	w_0	2.7 ± 0.1
Raleigh length [μm]	z_0	23 ± 3
Cavity decay rate [GHz]	κ	2.3 ± 0.9

Table 5.1: Cavity parameters. The reflectivity and the absorption is estimated under the assumption, that other losses like absorption or scattering can be neglected. ^a The parameter is visual determined from the camera images. ^b The parameter is determined from the transmission signal. ^c The parameter is the average value of the two independant measurements^{a,b} or an averaged value is used to calculate a further parameter.

compromise the equally weighted averaged value is taken as the result with $L = (27 \pm 8) \mu\text{m}$ and $\Delta\nu_{\text{FSR}} = (5.5 \pm 1.6) \text{THz}$. From the stability criterium defined in Eq. 2.16 this cavity is stable for a length $L \in \{(0 \mu\text{m}; 50 \mu\text{m}) \cap (500 \mu\text{m}; 550 \mu\text{m})\}$. The result of the cavity length is therefore in the expected order of magnitude.

The full width $\delta\nu$ is determined from the half width of the rising slope since an asymmetry in the resonance shape is observed which can be explained as follows. In Fig. 5.4 with a maximal resonance splitting the asymmetry between the rising slope of the first and the falling slope of the second resonance peak can be explained by a different rise and fall time of the photodetector, although it should be equal for this photodetector with $t_{r/f} = 14 \text{ns}$. Furthermore a small effect comes from the exponential decay of the cavity field and a limited bandwidth estimated in Eq. 5.1. In Fig. 5.4 the resonance splitting is within the spectral width and the asymmetry is significant larger because the amplitude of the left resonance is almost twice as large as the amplitude of the right resonance peak. This is possible by changing the ellipticity of the polarisation of the incoupled beam with the last $\lambda/2$ -plate in the setup. These effects mainly deform the falling slope and therefore only the half width of the rising slop is measured. For the calibration of the full width nonlinear effects of the piezo scan can be neglected since the width is in the same order of magnitude as the sideband difference.

5.4.2 Mirror reflectivity, mode waist and cavity decay rate

The reflectivity $R_{\mathcal{F}}$ is roughly estimated using Eq.(2.20) from the finesse under the assumption that losses like scattering and absorption can be neglected. For a more precise examination all

loss channels has to be considered, but they are not investigated in this work. Furthermore the mode waist w_0 , Raleigh length z_0 and the cavity decay rate κ can be estimated using Eq.(2.13),(2.11) and (2.21) from the known parameters, namely the radii of curvature of the mirrors, the cavity length, the free spectral range, the finesse and the reflectivity. The result is summarized with the other values in Tab. 5.1.

5.4.3 Resonance splitting

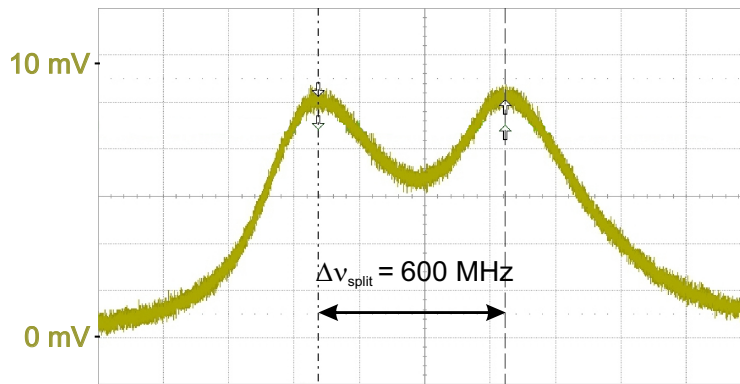


Figure 5.5: The resonance splitting caused by birefringence is observed in the transmission signal and the splitting depends on the birefringence of the mirror coating, the cavity length and the orientation of the two fibers against each other. For this cavity with a length of $27 \mu\text{m}$ the maximal splitting is $\Delta\nu_{\text{split}} = 600 \text{ MHz}$.

The resonance splitting explained in chapter 2.3.3 is measured from the transmission signal and as well calibrated by the two sidebands which are both in the same order of magnitude. In Fig. 5.6 the dependency of the splitting against the rotation angle of the MM fiber mirror around the cavity axes is shown. The uncertainty is determined by the standard deviation of the averaged quantity in each measurement. The uncertainty for the rotation angle is estimated to be $\pm 3^\circ$.

Discussion

The expected dependency between the orientation of the fiber mirrors against each other and the resonance splitting is observed. For a rotation of 360° , two minima and maxima are found.

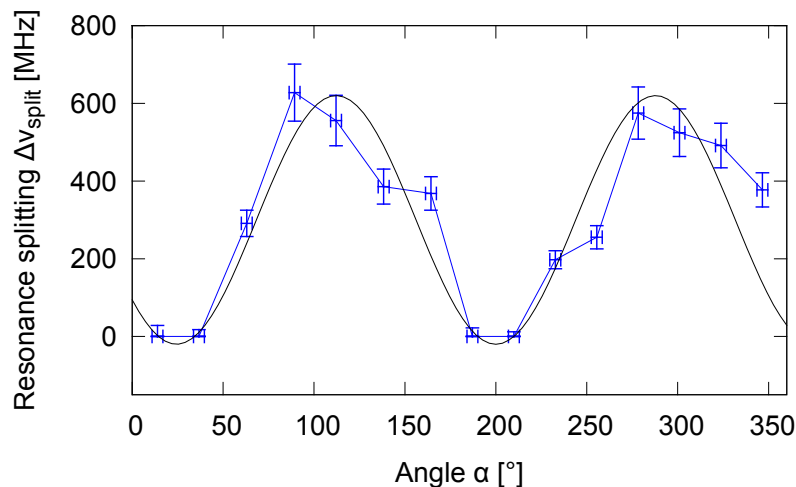


Figure 5.6: A sinusoidal dependency between the orientation of the fiber mirrors against each other and the resonance splitting is observed as the black solid line fit shows. For a rotation of 360° , two minima at almost zero and two maxima at 600 MHz are found.

The dependency follows a sinusoidal as the black solid line fit shows. The cavity with a length of $27\ \mu\text{m}$ has a maximal splitting of 600 MHz. The minimal splitting could not be determined as precisely, since the resonance peaks are indistinguishable within the resonance width. But by changing the amplitudes of both resonances one can determine, if the resonances are splitted indicated by a change of the signal asymmetry. From the fit the minimal splitting is close to zero which corresponds to an overlap of the two resonances.

5.4.4 Discussion

With this characterisation setup and this measurement method the main cavity parameters and the birefringence can be determined. Furthermore the setup can be improved by a more precise measurement of the cavity length or the free spectral range. One possibility is the measurement of the transmission by scanning the wavelength instead of the cavity. Another measurement method is the determination of the cavity length with the help of a second incoupled wavelength. This wavelength has to be close enough, that the different penetration depth into the dielectric mirror coating is negligible. For a cavity length which corresponds to the multiple of the least common multiple of half of both wavelength, the resonance peaks of both beams overlap. In this way the cavity length is determined within nanometer precision if the incoupled wavelength is precisely known. A further improvement of the measurement would be the decreasing of the large disturbances of the transmission signal due to vibrations and the air flow which can be realized with a shielding around the cavity.

Furthermore the parameters in chapter 5.4.2 are only roughly estimated. A more precise measurement, which consider all cavity losses, is the cavity ring down method as described in [10].

6 Summary

The demand for fiber cavities for studying light matter interaction increased in the recent years. The ablation setup in Paris is used as a basic tool for fabricating fiber mirrors by ablating material on a fiber end facet with a CO₂ laser. In this work we improved the controllability and the efficiency of the setup. A better quality of the CO₂ laser beam was achieved by the minimisation of the astigmatism caused by the dichroic mirror. This enables the adjustment of a certain beam radius by moving the fiber end facet along the beam direction. Therefore, the mirror can be removed during the ablation process in the future, if one finds a solution to place it reproducibly with nanometer precision at the same position between the lens and the fiber. The investigation of the CO₂ laser beam position between several ablation processes showed that the beam stays stable in time. After my work in Paris, they observed that the laser beam position was not stable during the production of around 100 fiber mirrors. Since I investigated the stability only for seven fiber mirrors during one day, a long term measurement can clarify this issue. The produced fiber end facets are characterised with two different profilometers. The low-cost Fizeau profilometer which is based on Newton rings is suitable to be implemented into the ablation setup while the Mirau profilometer can determine the structure with the precision of the coherence length of the used light source.

Based on the experiences in Paris, we built up an improved ablation setup in Bonn. The dichroic mirror and the microscope are substituted by a new alignment method of the fiber end facet. A 1550 nm laser is overlapped with the CO₂ laser beam and coupled into the fiber. By the amount of light coupled into the fiber, the position of the fiber is determined. As a new approach, a Michelson profilometer is implemented into the setup to determine the structure profiles on the fiber end facet. All electrical components in the ablation setup are controlled centrally with a MBED microcontroller which will enable an automated alignment of the fiber and ablation process in the future. Furthermore we will implement a fiber holder for the 390 fibers for an automated mass production. In a next step the setup needs to be characterized. Therefore, different profiles will be fabricated by varying the CO₂ laser power, the beam radius and the illumination time.

In a further experiment, the properties of a fiber cavity are investigated in Paris. Elliptically polarized light at a wavelength of 900 nm is coupled into the cavity and from the transmission signal as well as the camera pictures, the free spectral range, the finesse and the spectral width is determined. From this, the reflectivity of the mirrors, the mode waist and the cavity field decay rate are roughly estimated. Especially the birefringence of the mirror coating was also investigated in this measurement and is observed as a resonance splitting in the transmission signal. Here a dependency between the orientation of the fibers against each other and the splitting is found. The favoured goal is to overlap in this way the two resonances and circularly polarised light can be coupled into the cavity. Furthermore, one avoids in this case, that two modes couple to two different atom transitions or disturb the Doppler cooling. It would be interesting to observe how controllable the gluing of a cavity is since during the curing of the glue the mirrors can be slightly shifted against each other or additional external stress can change the birefringent effect.

As an experimental outlook, a new fiber cavity experiment is planned to be implemented in Paris as well as in Bonn to study the light-matter interaction under new conditions of the mode field. Therefore, new fiber mirrors will be fabricated with the improved ablation setups.

7 Appendix

A Circuit diagramm of the controlof the ablation process

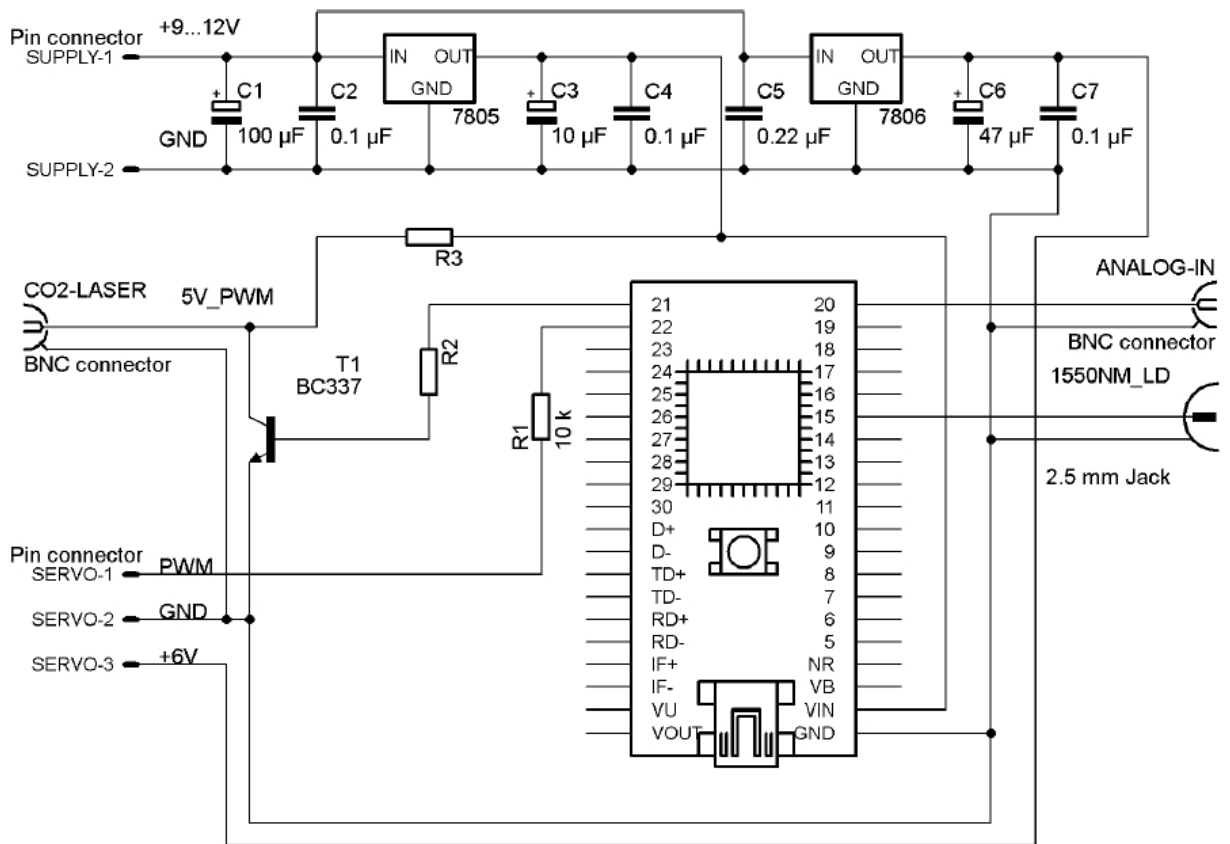


Figure A.1: The circuit diagram for the MBED and the devices in the ablation setup: The CO₂ laser, the 1550 nm laser diode, the shutter and the stages are all controlled by a single MBED microcontroller which is operated by a computer. Since the devices are in this way connected to each other, the full ablation process can be automatized.

References

- [1] PURCELL, E. M.: *Spontaneous emission probabilities at radio frequencies*. In: *Phys. Rev.* **69** (1946), S. 681
- [2] YE, J. ; VERNOOY, D. W. ; KIMBLE, H. J.: *Trapping of Single Atoms in Cavity QED*. In: *Phys.Rev. Lett.* **83** (1999), S. 4987–4990
- [3] RAAB, E. L. ; PRENTISS, M. ; CABLE, A. ; S.CHU ; PRITCHARD, D. E.: *Trapping of neutral sodium atoms with radiation pressure*. In: *Phys. Rev. Lett.* **59** (1987), S. 1800
- [4] METCALF, H. C. ; STRATEN, P. van d.: *Laser Cooling and Trapping of Neutral Atoms*. In: *Phys. Reports* **244** (1994), S. 203–286
- [5] MAUNZ, P. ; PUPPE, T. ; SCHUSTER, I. ; SYASSEN, N. ; PINKSE, P. W. H. ; REMPE, G.: *Cavity cooling of a single atom*. In: *Nature* **428** (2004), S. 50–52
- [6] THOMPSON, R. ; REMPE, G. ; KIMBLE, J.: *Observation of Normal-Mode Splitting for an Atom in an Optical Cavity*. In: *Phys. Rev. Lett.* **68** (1992), S. 1132–1135
- [7] BRUNE, M. ; SCHMIDT-KALER, F. ; MAALI, A. ; DREYER, J. ; HAGLEY, E. ; RAIMOND, J. M. ; HAROCHE, S.: *Quantum rabi oscillation: A direct test of field quantization in a cavity*. In: *Phys. Rev. Lett.* **76** (1996), S. 1800
- [8] KUHR, S. ; ALT, W. ; SCHRADER, D. ; DOTSENKO, I. ; MIROSHNYCHENKO, Y. ; ROSENFELD, W. ; KHUDAVERDYAN, M. ; GOMER, V. ; RAUSCHENBEUTEL, A. ; MESCHEDÉ, D.: *Coherence properties and quantum state transportation in an optical conveyor belt*. In: *Phys. Rev. Lett.* **91** (2003), S. 213002
- [9] KHUDAVERDYAN, M. ; ALT, W. ; KAMPSCHULTE, T. ; REICK, S. ; THOBE, A. ; WIDERA, A. ; MESCHEDÉ, D.: *Submicrometer position control of single trapped neutral atoms*. In: *Phys. Rev. Lett.* **95** (2005), S. 033003
- [10] DOTSENKO, I.: *Single atoms on demand for cavity QED experiments*, Rheinische Friedrich-Wilhelms Universität Bonn, Diplomarbeit, 2007
- [11] HUNGER, D. ; STEINMETZ, T. ; COLOMBE, Y. ; DEUTSCH, C. ; HÄNSCH, T. W. ; REICHEL, J.: *A fiber Fabry-Pérot cavity with high finesse*. In: *New J. Phys.* **12** (2010), S. 065038
- [12] STECK, D. A.: *Cesium D Line Data*. (1998)
- [13] AGRAWAL, G. P. ; KELLEY, P. L. (Hrsg.) ; KAMINOW, I. P. (Hrsg.) ; AGRAWAL, G.P. (Hrsg.): *Nonlinear fiber optics*. 3. Auflage. Elsevier Science, 2001
- [14] *From personal contact with THORLABS GmbH*
- [15] KITAMURA, R. ; PILON, L. ; JONASZ, M.: *Optical constants of silica glass from extreme ultraviolet to far infrared at near room temperature*. In: *Appl. Optics* **46** (2007), S. 8118–8133

-
- [16] DEUTSCH, C.: *High finesse fibre Fabry-Pérot resonators - Production, characterization and applications*, LMU München, Diplomarbeit, October 2008
- [17] FEIT, M. D. ; RUBENCHIK, A. M.: *Modeling of laser induced damage in NIF UV Optics*. In: *Lawrence Livermore National Laboratory CA (US)* (2001)
- [18] HUNGER, D. ; DEUTSCH, C. ; BARBOUR, J. ; WARBURTON, J. ; REICHEL, J.: *Laser micro-fabrication of concave, low-roughness features in silica*. In: *AIP Advances* **2** (2011), S. 012119
- [19] MENDEZ, E. ; NOWAK, K. M. ; BAKER, H. J. ; VILLARREAL, F. J. ; HALL, D. R.: *Localized CO₂ laser damage repair of fused silica optics*. In: *Appl. Optics* **45** (2006), S. 5358–5367
- [20] SIEGMANN, A. E.: *Lasers*. 55D Gate Five Road, Sausalito, CA 94965 : University Science Book, 1986
- [21] MESCHÉDE, D.: *Optik, Licht und Laser*. 3. Auflage. Vieweg + Teubner, 2008

Satutory decleration

I hereby certify that the work presented here was accomplished by myself and without the use of illegitimate means or support, and that no sources and tools were used other than those cited.

Bonn, October 31nd 2012

Acknowledgement

At first I want to thank Prof. Meschede and Prof. Reichel for introducing me into such a fascinating research field which inspired me so much that I will further work in this field in my PhD. The experiences were so special since I was able to work in two different groups as part of a cooperation. Also here I want to thank both for their support.

Furthermore I want to thank my advisor Marcel Spurny, who always found a way to support me in Bonn as well as in Paris. Every time I had a question, he found the time to help me.

I want to thank also both groups in Paris and in Bonn for the hours of helpful discussions. I found the work in both groups very pleasant which includes the work as well as the coffee breaks.

I finally want to thank Elisabeth Soergel who enabled the measurement of the mirror profile with the AFM.